



HAL
open science

An Unusual Reservoir of Water Emission in the VV CrA A Protoplanetary Disk

Colette Salyk, Klaus M. Pontoppidan, Andrea Banzatti, Ulrich Käuffl,
Cassandra Hall, Ilaria Pascucci, Andrés Carmona, Geoffrey A. Blake, Richard
Alexander, Inga Kamp

► **To cite this version:**

Colette Salyk, Klaus M. Pontoppidan, Andrea Banzatti, Ulrich Käuffl, Cassandra Hall, et al.. An Unusual Reservoir of Water Emission in the VV CrA A Protoplanetary Disk. *The Astronomical Journal*, 2022, 164, 10.3847/1538-3881/ac8878. insu-03860281

HAL Id: insu-03860281

<https://insu.hal.science/insu-03860281>

Submitted on 19 Nov 2022

HAL is a multi-disciplinary open access archive for the deposit and dissemination of scientific research documents, whether they are published or not. The documents may come from teaching and research institutions in France or abroad, or from public or private research centers.

L'archive ouverte pluridisciplinaire **HAL**, est destinée au dépôt et à la diffusion de documents scientifiques de niveau recherche, publiés ou non, émanant des établissements d'enseignement et de recherche français ou étrangers, des laboratoires publics ou privés.



Distributed under a Creative Commons Attribution 4.0 International License



An Unusual Reservoir of Water Emission in the VV CrA A Protoplanetary Disk

Colette Salyk¹, Klaus M. Pontoppidan², Andrea Banzatti³, Ulrich Käuffl⁴, Cassandra Hall^{5,6,7}, Ilaria Pascucci⁸,
Andrés Carmona^{9,10}, Geoffrey A. Blake¹¹, Richard Alexander⁷, and Inga Kamp¹²

¹Vassar College, 124 Raymond Avenue, Poughkeepsie, NY 12604, USA; cosalyk@vassar.edu

²Space Telescope Science Institute, 3700 San Martin Drive, Baltimore, MD 21218, USA

³Department of Physics, Texas State University, 749 N. Comanche Street, San Marcos, TX 78666, USA

⁴Josef-Raps-Strasse 5 D-80805, München, Germany

⁵Department of Physics and Astronomy, The University of Georgia, Athens, GA 30602, USA

⁶Center for Simulational Physics, The University of Georgia, Athens, GA 30602, USA

⁷School of Physics and Astronomy, University of Leicester, Leicester, LE1 7RH, UK

⁸Lunar and Planetary Laboratory, The University of Arizona, Tucson, AZ 85721, USA

⁹Université Grenoble Alpes, IPAG F-38000, Grenoble, France

¹⁰CNRS, IPAG F-38000, Grenoble, France

¹¹Division of Geological and Planetary Sciences, California Institute of Technology, Pasadena, CA 91125, USA

¹²Kapteyn Institute, PO Box 800, 9700 AV Groningen, The Netherlands

Received 2022 February 25; revised 2022 July 27; accepted 2022 August 8; published 2022 September 13

Abstract

We present an analysis of an unusual pattern of water vapor emission from the ~ 2 Myr old low-mass binary system VV CrA, as observed in IR spectra obtained with VLT-CRIRES, VLT-VISIR, and Spitzer-IRS. Each component of the binary shows emission from water vapor in both the L ($\sim 3 \mu\text{m}$) and N ($\sim 12 \mu\text{m}$) bands. The N -band and Spitzer spectra are similar to those previously observed from young stars with disks and are consistent with emission from an extended protoplanetary disk. Conversely, the CRIRES L -band data of VV CrA A show an unusual spectrum, which requires the presence of a water reservoir with high temperature ($T \gtrsim 1500$ K), column density ($N_{\text{H}_2\text{O}} \sim 3 \times 10^{20} \text{ cm}^{-2}$), and turbulent broadening ($v \sim 10 \text{ km s}^{-1}$) but very small emitting area ($A \lesssim 0.005 \text{ au}^2$). Similarity to previously observed water emission from V1331 Cyg and SVS 13 suggests that the presence of such a reservoir may be linked to evolutionary state, perhaps related to the presence of high accretion rates or winds. While the inner disk may harbor such a reservoir, simple Keplerian models do not match well with emitting line shapes, and alternative velocity fields must be considered. We also present a new idea, that the unusual emission could arise in a circumplanetary disk, embedded within the larger VV CrA A protoplanetary disk. Additional data are likely required to determine the true physical origin of this unusual spectral pattern.

Unified Astronomy Thesaurus concepts: [Protoplanetary disks \(1300\)](#); [Astrochemistry \(75\)](#); [Planet formation \(1241\)](#)

1. Introduction

The properties of planets are set by the physical and chemical conditions within the protoplanetary disks from which they form. Local disk chemistry may not only determine the bulk elemental composition of a planet (e.g., Grossman 1972) but also have profound effects on a wide range of planet properties. Whether or not ice is in solid form may drive planetesimal formation (Drażkowska & Alibert 2017), or increase surface densities sufficiently to allow for gas giant formation (e.g., Stevenson & Lunine 1988; Kennedy & Kenyon 2008). Interior and atmospheric chemistry can influence a planet's thermal evolution (e.g., Head & Solomon 1981), surface temperature (e.g., Kopparapu et al. 2013), and, ultimately, its suitability for life. However, it may not be possible to use ab initio chemico-dynamical models to reliably predict the planetary system that results from a given set of initial conditions. As recent Atacama Large Millimeter/submillimeter Array (ALMA) observations of rings, gaps, and spirals in disks reveal (e.g., Andrews et al. 2018), protoplanets and planets may already be present in intermediate-age “Class II” disks and are, themselves, influencing the disk environment. Thus, there is a mutual coevolution of

both the planet and the disk structure that will, in turn, affect the chemistry, potentially in chaotic ways (e.g., Salyk et al. 2015). Therefore, ground-truth observations of disk chemistry are required to establish how disk chemistry begins and how it evolves.

In particular, inner-disk ($R \lesssim 10$ au) chemistry can be studied with gas-phase IR spectroscopy, which probes the warm, molecular layer at relatively high disk altitudes (Najita et al. 2003). To date, the Spitzer InfraRed Spectrograph (IRS) has provided the majority of molecular detections (e.g., Carr & Najita 2008; Pontoppidan et al. 2010). This includes the detection of water vapor, a major molecular constituent of disks whose gas-phase abundance is influenced by such factors as the local radiation field and gas density (Du & Bergin 2014) and the radial transport of icy solids (Ciesla & Cuzzi 2006). However, Spitzer-IRS data are both spatially and spectrally unresolved, such that they reveal no kinematic information. Ground-based high-resolution spectroscopy is a powerful supplementary tool for locating the water and other molecules within the disk.

Much of the ground-based spectroscopic study of water vapor in disks (e.g., Banzatti et al. 2017) has been performed with the CRYogenic high-resolution InfraRed Echelle Spectrograph (CRIRES; Kaeuffl et al. 2004) on the Very Large Telescope (VLT). Mid-IR water emission has been studied previously with Michelle (Glasse et al. 1997) and TEXES (Lacy et al. 2002), confirming that the mid-IR emission lines



Original content from this work may be used under the terms of the [Creative Commons Attribution 4.0 licence](#). Any further distribution of this work must maintain attribution to the author(s) and the title of the work, journal citation and DOI.

Table 1
CRIRES Observing Log

Obs. ID	UT Date	λ_{ref} (μm)	PA (deg)	Exp. Time (s)	Calibrator	Setting
200165762	2007-04-25	4.7160	45	600	BS 5646, BS 6879, BS 7236	M
200165762	2007-04-25	4.7300	45	600	BS 5646, BS 6879, BS 7236	M
200165762	2007-04-25	4.8400	45	300	BS 5646, BS 6879, BS 7236	M
200168547	2007-08-30	2.9515	44	720	BS 6084, BS 7236, BS 7337	H ₂ O
200168547	2007-08-30	2.9650	44	500	BS 7236, BS 7337	H ₂ O
200168547	2007-08-30	3.7170	44	360	BS 7236, BS 7337	organics
200168597	2007-08-31	3.6100	44	600	BS 7236	organics
200168597	2007-08-31	3.6200	44	600	BS 7236	organics
200168597	2007-08-31	3.7040	44	600	BS 7236	organics
200168649	2007-09-01	2.3730	44	800	BS 7236, HIP 101589	K
200168649	2007-09-01	2.3780	44	560	BS 7236, HIP 101589	K
200168649	2007-09-01	4.7700	44	960	BS 7236	M
200168649	2007-09-01	4.7795	44	960	BS 7236	M
200169023	2007-09-06	3.4565	44	360	BS 7913	organics
200169023	2007-09-06	3.5350	44	360	BS 7913	organics
200179090	2008-08-10	4.9462	44	480	BS 7236	M

arise from disk surfaces within the water snow line (Salyk et al. 2019). More recently, we have executed a large survey of water vapor in the mid-IR (*N*-band) regime with the VLT Imager and Spectrometer for the mid-InfraRed (VISIR; Lagage et al. 2004; Käufel et al. 2015).

One avenue of disk chemistry that remains relatively unexplored is chemistry in binary (or multiple) systems, as well as understanding the interaction between disk chemistry and companions, including protoplanets. To what extent does the presence of companions affect chemistry? Do disks in multiple systems, which both are coeval and derive from the same initial conditions, develop the same disk chemistry? The latter question provides a powerful test of the extent to which disk (and therefore planetary) chemistry is deterministic or stochastic. It was with these questions in mind that we added the binary VV CrA to our spectroscopic survey. VV CrA is a ~ 2 Myr old (Sullivan et al. 2019) $2''1$ binary located in the Corona Australis star-forming region, at a distance of 157 pc (GAIA DR3; Gaia Collaboration et al. 2016, 2021). It is associated with a Herbig-Haro object (Wang et al. 2004). The SW component is of type M1 and dominates at visible wavelengths. The NE component, of type M0, is faint at visible/near-IR wavelengths but has dominated in the thermal IR at some epochs (Avilez et al. 2017) and has therefore in some references been classified as an IR companion (IRC; Koresko et al. 1997). The photospheric spectroscopy and modeling of Sullivan et al. (2019) suggest that the SW and NE stellar components have masses of ~ 0.55 and $0.45 M_{\odot}$, respectively. Following the conventions of previous authors, we will refer to the SW component as the primary star (VV CrA A) and the NE component as the secondary IRC (VV CrA B). VV CrA A is inclined by 32° (Gravity Collaboration et al. 2021), but the geometry of the two disks relative to each other is still under debate; quantitative analyses of absorption features from CO (Smith et al. 2009) and silicates (Kruger et al. 2011) suggest that the light from the secondary may be absorbed by the disk of the primary.

In this paper, we analyze multi-instrument, ground-based high-resolution ($\lambda/\Delta\lambda = R \sim 30,000$ – $95,000$) and Spitzer-IRS Short- and Long-High ($R \sim 500$) IR spectra of an unusual pattern of water vapor emission from the protoplanetary disks in the VV CrA system. Section 2 presents spectra from

VLT-CRIRES, VLT-VISIR, and Spitzer-IRS, covering wavelengths from 2.3 to 35 μm . The ground-based VLT spectra spatially resolve the binary to yield separate spectra for each component. In Section 3, we discuss the results of our analysis and model the spectra using both a simple slab model and a more detailed two-dimensional compact disk model. The analysis demonstrates evidence for a compact source of water vapor emission in VV CrA A, with high temperature, column density, and turbulent velocity. Finally, in Section 4, we discuss possible physical origins for the water reservoir, including a circumplanetary disk, and related implications.

2. Observations and Data Reduction

2.1. CRIRES 2–5 μm High-resolution Spectroscopy

Near-IR (2–5 μm), high-resolution ($\lambda/\Delta\lambda \sim 95,000$) spectra were obtained with CRIRES (Käufel et al. 2004) on the European Southern Observatory (ESO) VLT, as part of programs 179.C-0151 (PI: van Dishoeck) and 082.C-0432 (PI: Pontoppidan).

Data were reduced using IDL routines described in Pontoppidan et al. (2011). Reduction steps included nod subtraction, trace linearization, optimal extraction, and wavelength calibration with telluric emission lines. All wavelengths were converted to heliocentric values. Telluric calibration was performed with division by observed A- and B-type star telluric calibrators, whose near-IR spectra are relatively featureless. As a final step, spectra in adjacent wavelength settings were combined together into one of four settings: “K,” “H₂O,” “organics,” or “M.” The complete wavelength coverage of the four settings is 2.3382–2.3964 μm , 2.9051–2.9897 μm , 3.3983–3.7495 μm , and 4.6457–4.9940 μm , respectively. The “H₂O” and “organics” settings are both in the “L” filter, so we refer to these collectively as “L-band” spectra in the remainder of the text. An observing log for the CRIRES spectra is provided in Table 1.

Due to the narrow slit ($0''.2$) of CRIRES, the spectra cannot be accurately calibrated to an absolute flux density scale. Consequently, we scale the VV CrA A spectra to Wide-field Infrared Survey Explorer (WISE) photometry (24 W1 measurements of the sum of the two VV CrA components between 2010 April and September, average W1 = 4.38 mag), coupled

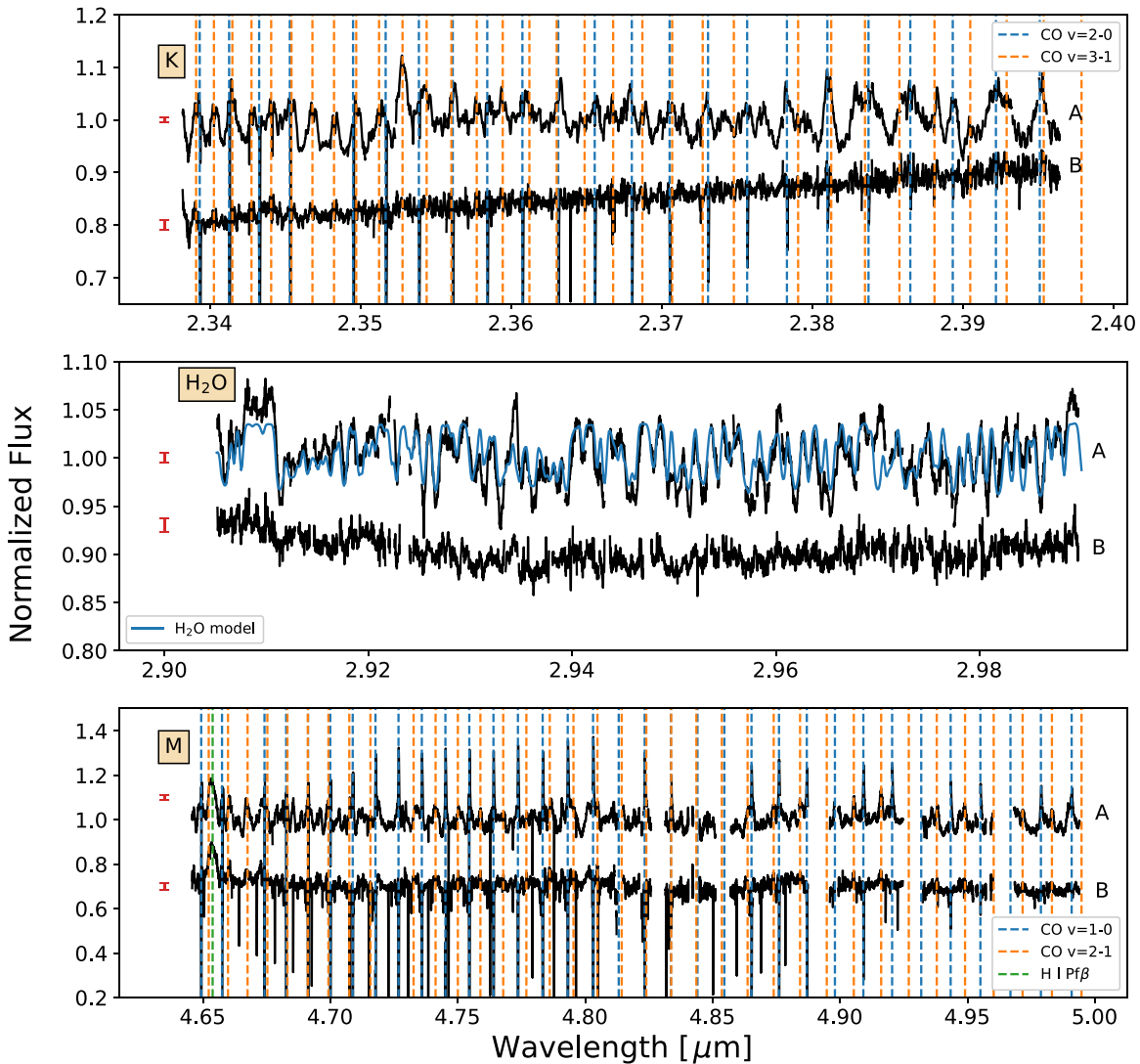


Figure 1. CRILES spectra of VV CrA A (top curves) and B (bottom curves) in the “K” (top), “H₂O” (middle), and “M” (bottom) settings. Dashed vertical lines mark prominent ¹²CO and H I transitions. Emission features from VV CrA A in the “H₂O” setting are due to numerous blended vibrational water transitions; the blue curve shows our nominal water slab model, discussed in Section 3.1. Representative errors (which we estimate to be ~ 3 times the statistical error) are shown on the left.

with a flux density ratio between VV CrA A and B at L' of 1.01 (Sullivan et al. 2019), obtained on 2015 July 12. However, it is known that VV CrA is variable in the mid-IR at the $\sim 30\%$ level on a 10 yr timescale (Kóspál et al. 2012). The WISE light curve indicates variability of 20% on a 6-month timescale.

A representative overview of the CRILES spectra is shown in Figure 1, and the full data set is displayed in the Appendix (Figures A1–A4).¹³ M -band data for VV CrA B were previously analyzed by Smith et al. (2009), and M -band data for both sources were previously discussed by Bast et al. (2011).

2.2. VISIR 12 μ m High-resolution Spectroscopy

VV CrA was observed with the VISIR spectrograph (Lagage et al. 2004; Käufel et al. 2015) on the VLT, as part of the large program 198.C-0104 (PI: Pontoppidan). Spectra were obtained using the high-resolution mode, with a resolving power of $R \sim 30,000$.

Both components of VV CrA were observed in 2017 April in three wavelength settings: one setting centered at 12.414 μ m, covering rotational water lines; one centered at 12.27 μ m, containing OH and the H₂ S(2) line; and one centered at 12.837 μ m, containing the [Ne II] line. The [Ne II] data were previously analyzed in Pascucci et al. (2020) and will not be discussed in this work. Asteroids (6) Hebe and (10) Hygiea were observed as telluric calibrators. For the 2017 April observations of VV CrA, the slit was oriented along the binary position angle (PA), and both targets were observed simultaneously. On 2017 September 08, VV CrA was observed again at two different PAs, separated by 180°, in order to perform spectro-astrometry. An observing log for VISIR is shown in Table 2.

Spectra were reduced using Python developed by our team. Reduction steps included nod subtraction, trace linearization, optimal extraction, and wavelength calibration using telluric emission lines. To remove telluric absorption features, both source and standard spectra were fit by a molecfit (Kausch et al. 2015; Smette et al. 2015) model, which was subsequently divided into each spectrum. The atmospheric-corrected source

¹³ Reduced data are also available at <https://www.stsci.edu/~pontoppi/#data>.

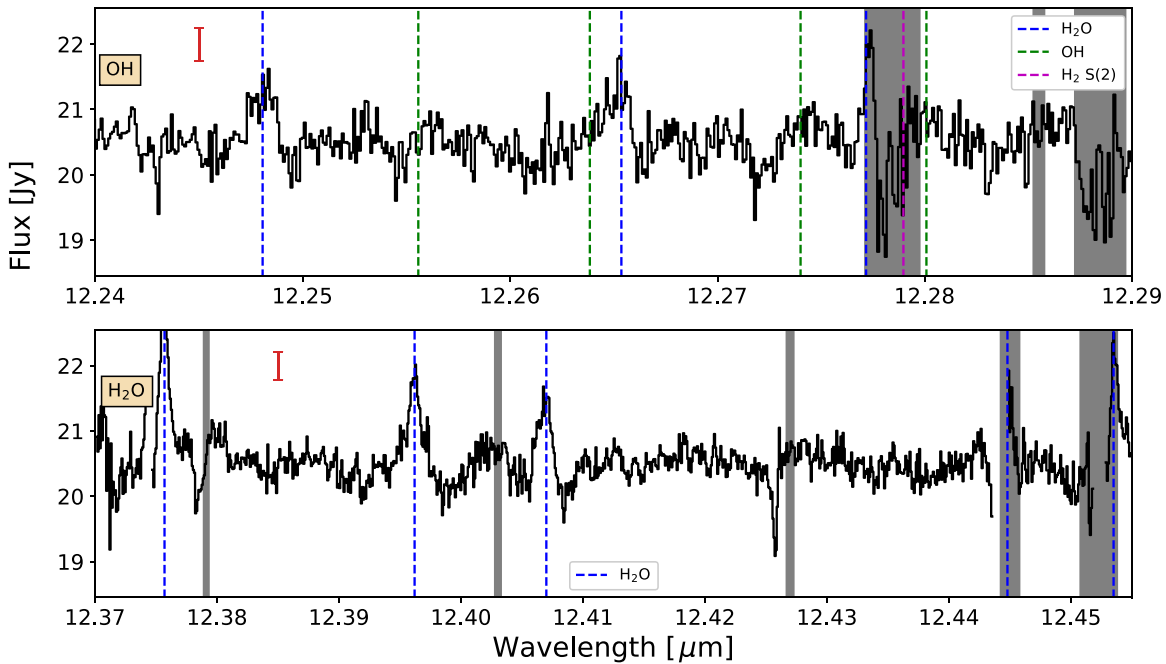


Figure 2. Reduced spectra of VV CrA in the two water/OH settings observed with VISIR. Gray rectangles mark regions with atmospheric transmission less than 80%. Dashed lines mark the theoretical locations of H₂O, OH, and H₂ transitions. Data wavelengths are heliocentric, and theoretical wavelengths have been shifted by -1 km s^{-1} , the VV CrA stellar velocity (Fang et al. 2018). In the upper left corner, we show representative error bars computed from the standard deviation of flat spectral regions.

Table 2
VISIR Observing Log

Obs. ID	UT Date	λ_0 (μm)	PA (deg)	Exp. Time (s)	Calibrator	Setting
1732798	2017-04-25	12.414	136	1890	(6) Hebe	H ₂ O
1733361	2017-04-26	12.270	136	1800	(6) Hebe	OH
1733364	2017-04-26	12.837	0	1800	(6) Hebe	[Ne II] ^a
1830517	2017-09-08	12.414	136	2160	(10) Hygiea	H ₂ O
1830520	2017-09-08	12.414	-44	2160	(10) Hygiea	H ₂ O

Note.

^a See Pascucci et al. (2020).

was then divided by the atmospheric-corrected standard to produce the final spectrum. The use of an atmospheric model helps account for differences in telluric absorption between source and standard, while the use of the asteroid as telluric calibrator corrects for any instrumental effects, as described further in Mandell et al. (2011). Finally, spectra were fringe-corrected using low-order polynomials and flux-calibrated using the flux density measured through the Si-6 ($12.33 \mu\text{m}$) VISIR bandpass from Kruger et al. (2011). Figure 2 shows the reduced VISIR spectra in the three settings.

Spectro-astrometric (SA) measurements in the $12.414 \mu\text{m}$ water setting are shown in Figure A5. A detailed discussion of the SA method can be found in Pontoppidan et al. (2011). In short, spectro-astrometry is a measurement of the spatial centroid of the emission as a function of wavelength. This spatial centroid is expected to vary with wavelength, as the blueshifted part of a Keplerian disk is spatially offset from the redshifted part. Since the measured location of the centroid is influenced by instrument- and sky-induced residuals, the object is observed at two antiparallel PAs, and the calibrated SA signal is constructed by subtracting the SA offsets of the two

PAs (in this case, 136° and -44°) and dividing by two. With this method, instrument- and sky-induced residuals cancel out, and only source-based signals remain. Based on empirical tests aimed at maximizing the signal-to-noise ratio (S/N), we used a 12-pixel-wide box to calculate the spatial centroid. Because the SA extraction box truncates the point-spread function, an empirically determined correction factor of 1.2 was applied to the final SA spectrum.

2.3. Spitzer 10–35 μm Medium-resolution Spectroscopy

VV CrA was observed with Spitzer-IRS (Houck et al. 2004) in the $9.9\text{--}19.6 \mu\text{m}$ short-high (SH) and $18.7\text{--}37.2 \mu\text{m}$ long-high (LH) modules as part of program 20611 (PI: Wright). In this work, we use the archival data from program 20611 (AOR 14921984), but re-reduced following the steps described in Pontoppidan et al. (2010). The VV CrA binary was not spatially resolved by IRS, so the spectra represent the sum of the two targets. The continuum-subtracted IRS SH and LH spectra are shown in Figure 3.

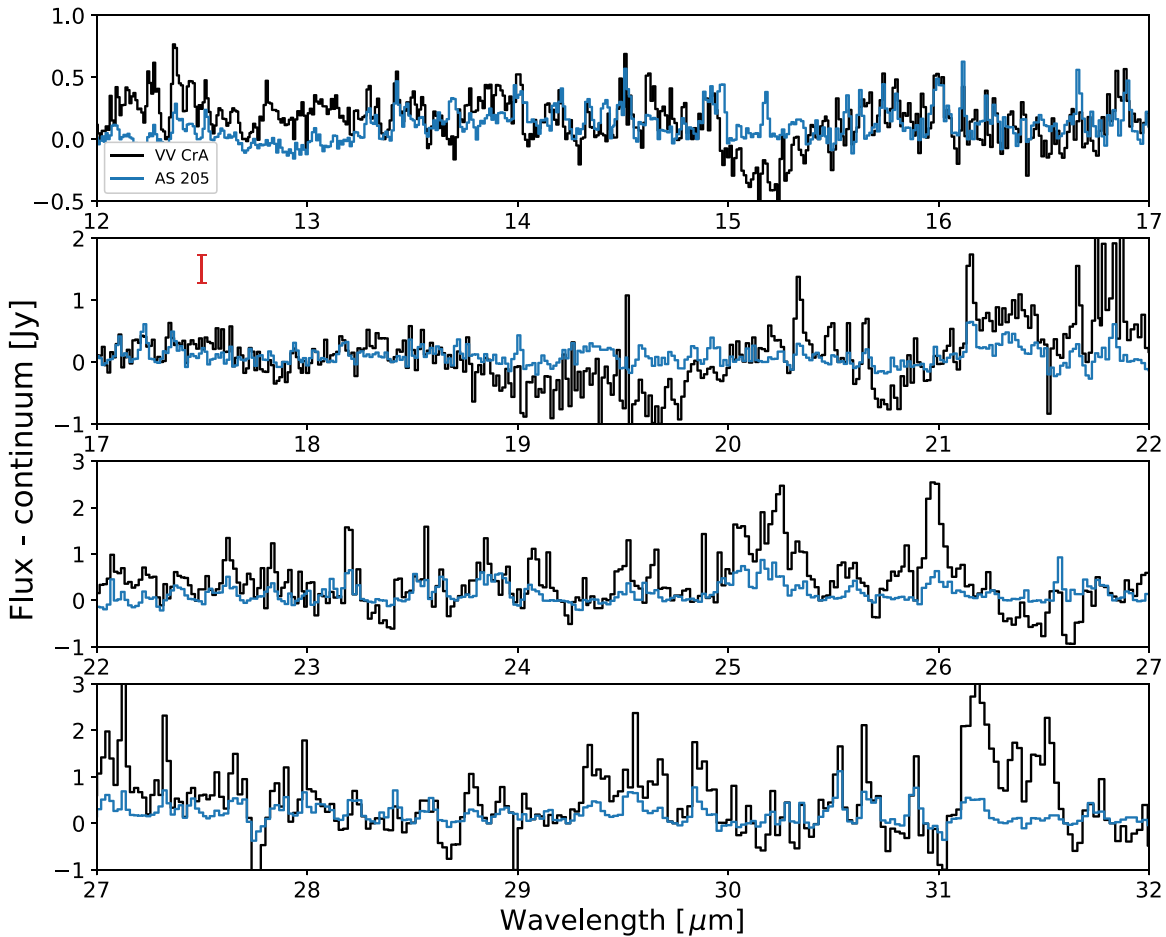


Figure 3. Continuum-subtracted Spitzer-IRS high-resolution spectra of VV CrA (A and B combined; black) and the water-rich disk AS 205 (blue; Pontoppidan et al. 2010), for comparison. A representative error bar is shown in the second panel, computed from the standard deviation between 17 and 18 μm .

3. Analysis

3.1. Evidence for an Unusual Compact, Hot, and Dense Water Reservoir

The CRIREs L -band spectrum of VV CrA A (Figures 1, A2, and A3) is characterized by a dense forest of lines from rovibrational transitions of water vapor. While the observed spectrum covers only parts of the atmospheric L -band window, water lines are observed at nearly all covered wavelengths, including the range around 3 μm , where water vapor emission is commonly seen in protoplanetary disks (Banzatti et al. 2017), but also out to the red end of the spectral coverage at 3.75 μm . The extension of the 3 μm water stretching-mode band to such long wavelengths is unusual, appearing similar to only one previously studied disk, V1331 Cyg (Doppmann et al. 2011), which we discuss further in Section 4. Overall, we inspected 37 L -band spectra of protoplanetary disks and did not note another similar spectrum.¹⁴

The spectral extent of the observed water band in VV CrA A suggests that unusually high temperatures and/or unusually high column densities are present. Further, the fact that the water lines have roughly constant strength (~ 0.1 – 0.2 Jy) across a band that includes transitions with a wide range of upper level energies (~ 5000 – $10,000$ K) and strengths (< 0.01 – 90 s $^{-1}$)

suggests that they are optically thick, which would also imply high column densities.

In the following, we investigate the properties of the emitting material required to reproduce the observed water spectrum in VV CrA A, and we discuss which unusual circumstances may be required to explain it. We use both a simple slab model and a more detailed two-dimensional radiative transfer model to estimate gas temperature, column density/abundance, and emitting area.

3.2. Slab Model of the VV CrA A Water Emission

We investigated the VV CrA A “H₂O” spectrum with the use of a simple slab water emission model (“slabspec”; Salyk 2020), which consists of a slab of water vapor with a single temperature (T), column density ($N_{\text{H}_2\text{O}}$), and emitting area (A). Emission-line data come from the HITRAN database (Gordon et al. 2017). The model also has a tunable parameter setting the standard deviation of the local Gaussian line broadening (ν), which serves as a parameterization of the local turbulent velocity. We then convolved all of the model spectra with a Gaussian with an FWHM of ~ 30 km s $^{-1}$ ($\sigma = 12.7$ km s $^{-1}$) to match the appearance of the observed spectra. This step represents nonlocal broadening due to Keplerian motion and, potentially, non-Keplerian outflows or winds. (A more detailed investigation of line shapes is described in Section 3.3.)

We explored a range of values for $N_{\text{H}_2\text{O}}$, T , and ν to derive a nominal model that fits the rovibrational water lines in the

¹⁴ The spectra had a range of S/Ns and a range of line-to-continuum ratios for water emission, including nondetections, so the detection rate should not be taken to be the same as the occurrence rate.

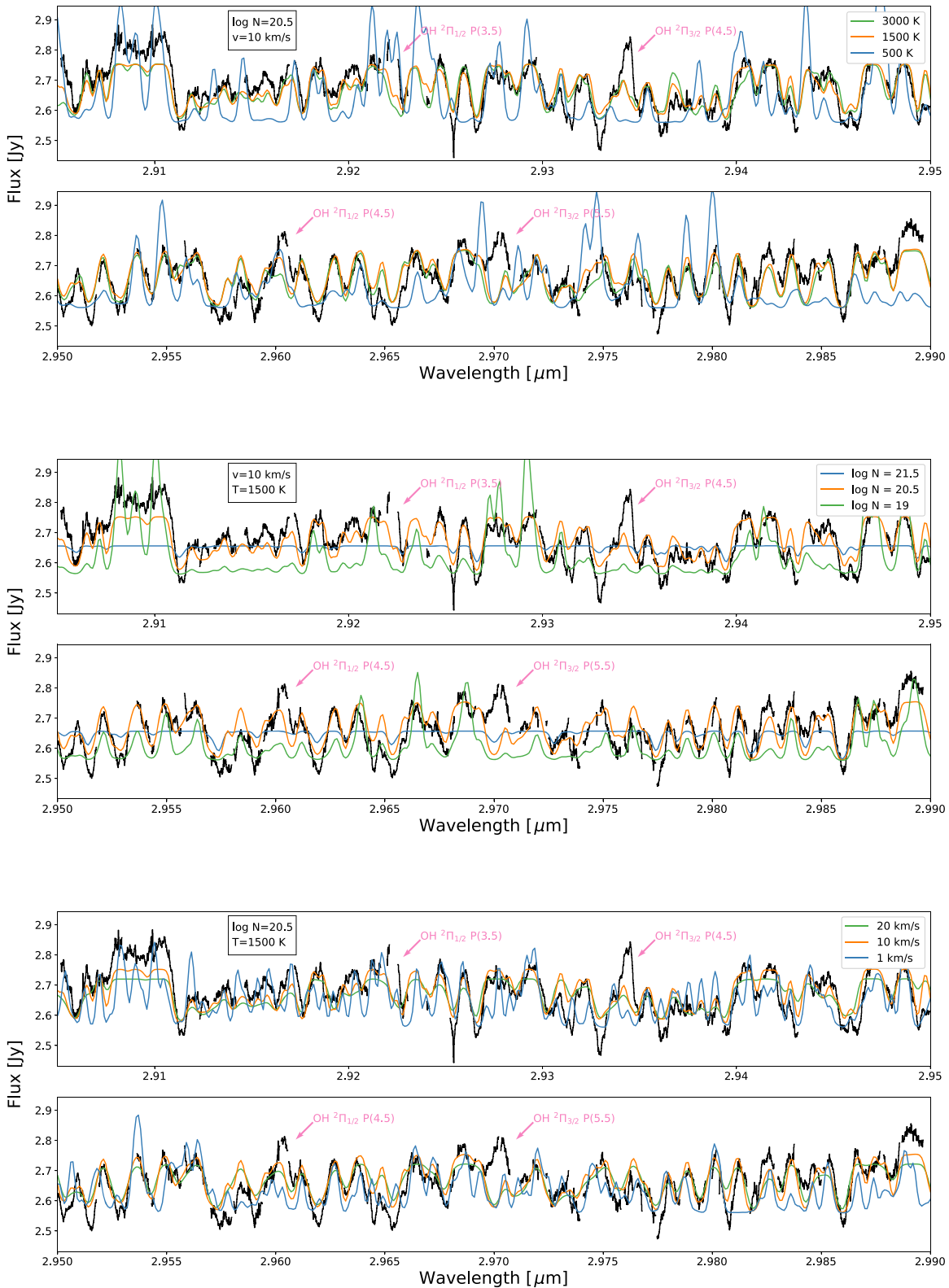


Figure 4. Water vapor slab models with different values of temperature (top), water column density (middle), and line broadening (bottom), as compared to CRIRCS data for VV CrA in the “H₂O” setting. Arrows mark probable OH emission features. Boxes in the upper left corner list fixed model parameters.

“H₂O” setting. Since changes to the emitting area scale the entire spectrum linearly by a constant factor, we adjusted this factor after choosing $N_{\text{H}_2\text{O}}$, T , and v , such that the value of emitting area minimized the sum of squared residuals. Our nominal model is taken to have $T = 1500$ K,

$N_{\text{H}_2\text{O}} = 3 \times 10^{20} \text{ cm}^{-2}$, $v = 10 \text{ km s}^{-1}$, and $A = 0.003 \text{ au}^2$ —see Figure 4, orange curves. Throughout the remainder of the text, we refer to this as our nominal L-band slab model. Figure 5 shows a breakdown of the nominal model into contributing emission lines over a portion of the spectrum,

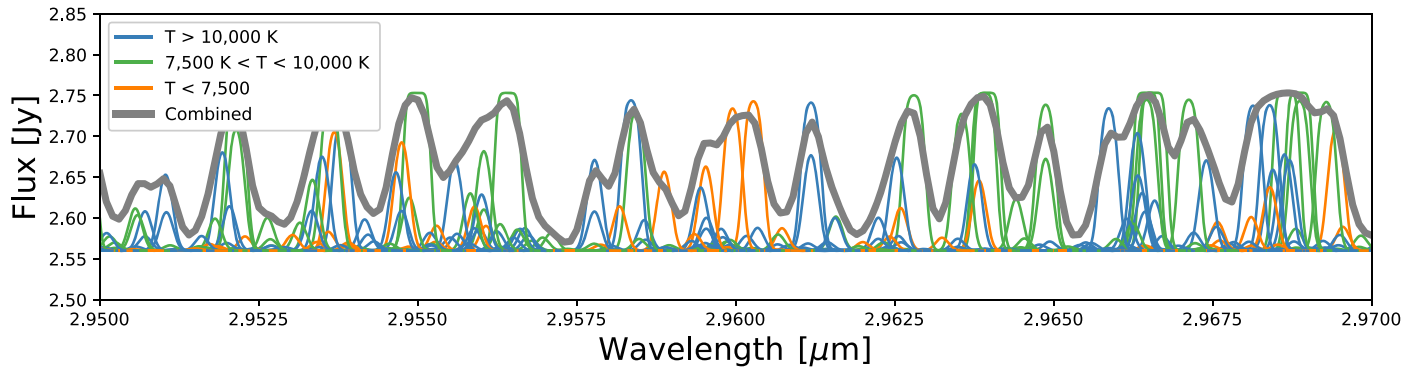


Figure 5. Breakdown of a portion of our nominal model into its component individual emission lines. Color-coding shows the excitation temperature of the upper levels. The thick gray curve shows the combined, convolved model.

demonstrating the high excitation temperatures of the emitting lines and the complexity of the resulting spectra.

Figure 4 shows how each of the free parameters affects the model. Temperature and column density both affect the relative line strengths, with higher temperatures adding flux in higher-excitation lines and higher column densities adding flux in weaker lines. Column density and local line broadening both affect the broadness of optically thick lines; an increased column density increases optical depths at all velocities, while an increased local line broadening redistributes molecules to a wider range of velocities. However, the effects of increasing column density and local line broadening are different—at high column densities ($N_{\text{H}_2\text{O}} \sim 10^{23} \text{ cm}^{-2}$), models approach the flat blackbody optically thick limit for all wavelengths, whereas with large line broadening, optically thick lines develop flat shapes, while optically thin lines only broaden slightly.

Figure 6 shows the relative goodness of fit for a model grid with different values of $N_{\text{H}_2\text{O}}$, T , and v , where we define the relative goodness of fit as the sum of squared residuals divided by that of the best-fit model. (None of the models can perfectly match all of the spectral features, so reduced- χ^2 values remain high for all models.) Residuals were computed between 2.905 and 2.99 μm , excluding regions near known OH emission lines, and for each set of $N_{\text{H}_2\text{O}}$, T , and v , we adjusted the emitting area to minimize the sum of squared residuals. We see that high temperatures ($T \gtrsim 1500 \text{ K}$) and high local line broadening ($v \gtrsim 10 \text{ km s}^{-1}$) are preferred, but the upper limits of these parameters are not well constrained. Best-fit models have column densities of $N_{\text{H}_2\text{O}} = (1 - 3) \times 10^{20} \text{ cm}^{-2}$. Associated emitting areas are $\lesssim 0.005 \text{ au}^2$, with smaller emitting areas corresponding to higher temperatures, and vice versa.

Note that the best-fit emitting area is not necessarily equal to the size of the region containing water vapor, as lower-temperature water vapor will not effectively emit at these wavelengths. Furthermore, when our nominal L -band slab model is applied to the broader L -band wavelength range (i.e., the wider “organics” setting), it predicts emission weaker than that observed. When extrapolated to the longer wavelengths covered by VISIR and Spitzer, it also greatly underpredicts observed emission lines. This is further evidence that water vapor exists at a range of temperatures. We consider this further in Sections 3.4 and 3.5.1.

3.3. Velocity of the Water Vapor

The velocities of the L -band emission lines can be used to constrain the emitting location of the hot, compact emitting

region. Hot emission lines can naturally be produced near the inner edge of a protoplanetary disk. However, as discussed in Section 3.2, convolution with an $\text{FWHM} \sim 30 \text{ km s}^{-1}$ ($\sigma = 12.7 \text{ km s}^{-1}$) line shape matches the appearance of the data. As we will discuss, these widths may be too narrow to explain with a standard protoplanetary disk model.

In Figure 7, we show how the location and shape of the compact emitting region affect the appearance of the observed spectrum. We constructed a model from a ring of constant irradiance (i.e., equivalent to a single-temperature blackbody) with emitting area 0.003 au^2 , which we then oriented at an inclination of 32° (Gravity Collaboration et al. 2021) to produce a line shape. To compare with the data, we then took the (unconvolved) spectrum output by our nominal slab model (see Section 3.2) and convolved it with the line shape model.

In the first model, as shown in the top left panel of Figure 7, we considered a ring beginning at the measured dust inner radius of $\sim 0.17 \text{ au}$ (Gravity Collaboration et al. 2021), extending to 0.173 au (to match the slab model emitting area), orbiting a $0.55 M_\odot$ star. This model produces a wide, double-peaked line profile; when convolved with the slab model, it flattens out the spectrum such that it does not well match the data. It has been observed by, e.g., Bast et al. (2011) that molecular disk emission-line profiles are sometimes non-Keplerian, so we also consider a Lorentzian profile matching the observed CO M -band line shape, with line wings consistent with inner disk velocities. This, too, produces a spectrum flatter than observed.

In a second model (Figure 7, middle panel), we arbitrarily set the disk inner radius to 0.9 au to match the observed line widths. The narrower resulting line profile matches the observed data when convolved with the slab model; however, it requires the adoption of a very thin ($\Delta r = 6 \times 10^{-4} \text{ au}$), hot ring to match the slab model emitting area. The ring location conflicts with the measured dust rim location of $0.17 \pm 0.02 \text{ au}$ (Gravity Collaboration et al. 2021). But perhaps the high UV radiation flux around this rapidly accreting ($\dot{M} = 3 \times 10^{-7} M_\odot \text{ yr}^{-1}$; Fang et al. 2018) star causes photo-dissociation of H_2O out to larger radii (Bethell & Bergin 2009). It is unclear, however, how to produce such a narrow ring of hot water, and it may be difficult to reconcile the high gas temperatures with the expected equilibrium temperature of 470 K at 0.9 au around a $4.9 L_\odot$ star.

As a third model, we considered the idea that the narrow lines, high column density, and small emitting area might be explained by a *circumplanetary* disk (CPD) around a massive, young planet or substellar companion. To test this option, we

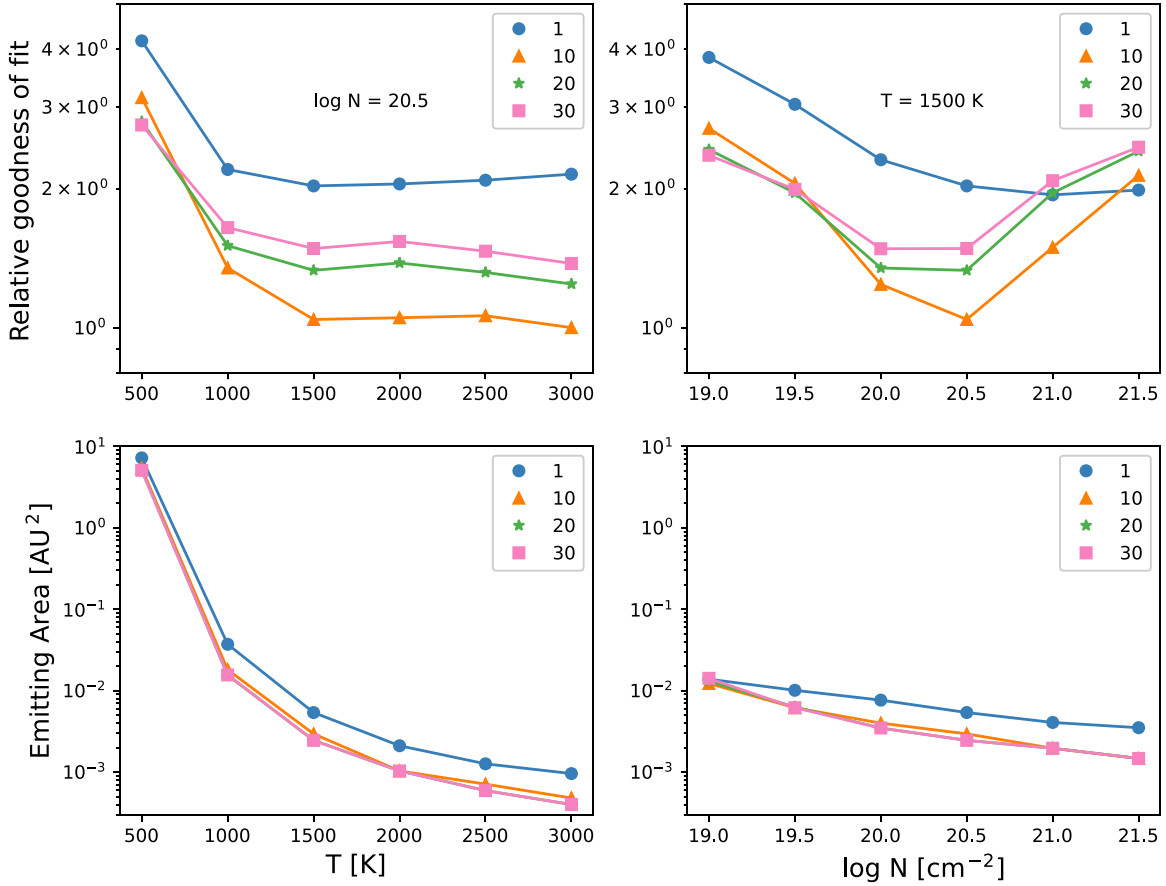


Figure 6. Top: relative goodness of fit (residual sum of squares divided by that of the best-fit model) for a range of model parameters. The top left panel shows the dependence of goodness of fit on temperature, with $N_{\text{H}_2\text{O}}$ fixed at $3 \times 10^{20} \text{ cm}^{-2}$, while the top right panel shows the dependence on column density, with T fixed at 1500 K. Different colors and symbols show different values of the local line broadening, v , in km s^{-1} . Bottom: corresponding emitting areas for each model.

constructed a model for a disk around a $6M_J$ planet, with an inner radius of $10R_J$ extending to $60R_J$ (discussed further in Section 3.4). As shown in Figure 7 (bottom panel), a CPD also produces a narrow line profile consistent with the data and will match the emitting area with a more plausible range of disk radii. This concept is developed further with a two-dimensional model in Section 3.4.

One important, potential difference between a CPD and a narrow ring within a protoplanetary disk is that the CPD lines will be offset owing to the Keplerian velocity of the planet. The magnitude of the offset may range from 0 (if the planet is on the far or near tangent of its orbit) up to $v_{\text{CPD, Kepler}} \sin(i)$, where i is the inclination of the CPD orbit around VV CrA A. As a representative example, we show an offset of $\sim 4 \text{ km s}^{-1}$, given by the Keplerian speed around a $0.55 M_\odot$ star of a “Jovian” orbit at 5 au, projected to $i = 32^\circ$ and an azimuth of 45° . The actual semimajor axis of any putative CPD is unknown.

To test this idea, we compared the L -band water emission to the stellar velocity. Fang et al. (2018) find a heliocentric stellar velocity of $-1 \pm 0.3 \text{ km s}^{-1}$ for VV CrA A. For the L -band data, lines cannot be separated, so we estimated the velocity by two methods: minimization of χ^2 between our slab model and data, which finds a best-fit velocity of 4 km s^{-1} , and a cross-correlation between slab model and data, which suggests a velocity of -1 km s^{-1} . Therefore, given systematic errors of a few kilometers per second, we find no significant difference between the stellar and L -band water velocities. Future work

would need to more carefully reduce systematics to check for velocity offsets consistent with a CPD. We note, however, that offsets greater than $5\text{--}10 \text{ km s}^{-1}$ with respect to the stellar velocity are not consistent with our data.

In summary, we show that the observed fluxes and velocities are consistent with either a thin ring far from the star or a compact spot, e.g., a circumplanetary disk. We consider the CPD hypothesis further in the next section.

3.4. Two-dimensional Radiative Transfer Model of a Circumplanetary Disk

In this section, we discuss more sophisticated modeling we performed to further explore the possibility that the L -band emission arises in a CPD. We utilized the radiative transfer modeling code RADMC (Dullemond & Dominik 2004) coupled with the line radiative transfer code RADLite (Pontoppidan et al. 2009). As indicated by the slab model, the water emission appears to be formed in a small emitting area with high excitation temperature, large column densities, and a high degree of turbulent broadening.

Figure 8 shows a portion of a nominal RADLite model that provides a good match to the L -band data. The full wavelength coverage can be seen in Figures A1–A4. The RADLite model calculations of the full spectral range are too time-consuming to investigate uniqueness, so this represents one plausible solution.

In this model, the disk surrounds a $6M_J$ planetary companion. The radius and effective temperature of the central object

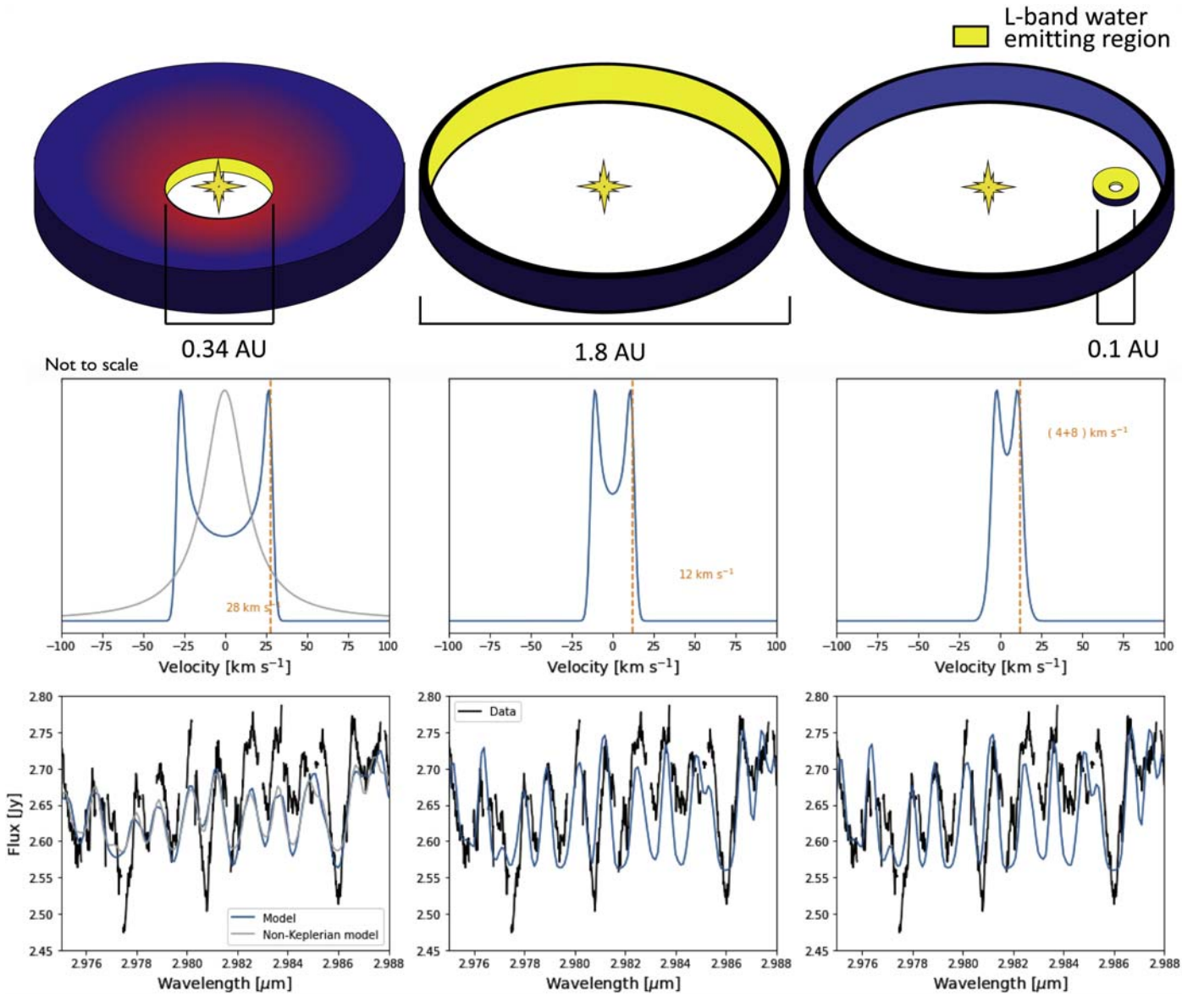


Figure 7. Representative drawings (top; not to scale), line shapes (middle), and resultant spectra (bottom) for the three *L*-band water emission models discussed in Section 3.3. Left: a ring at the dust inner radius of 0.17 au, surrounding a $0.55 M_{\odot}$ star with a Keplerian (blue) or non-Keplerian Lorentzian (gray) line profile. Middle: a ring at 0.9 au, surrounding a $0.55 M_{\odot}$ star. Right: a circumplanetary disk surrounding a $6M_J$ planet, offset by 4 km s^{-1} . All models are inclined by 32° .

determine its luminosity, which affects the strength of the emission lines, but do not otherwise change the appearance of the spectrum. We find that a CPD surrounding a $5R_J$ planet, with an effective temperature of 3200 K, corresponding to a luminosity of $0.023 L_{\odot}$, can generate an H_2O spectrum with similar line strengths to the observed spectrum. However, other combinations of radius and effective temperatures are similarly allowed as long as the total luminosity is kept roughly constant. The disk is required to have a very high gas-to-dust ratio of 70,000 and high water abundance relative to H_2 of 0.05 to reach the observed optical depths. The disk is assumed to have an inner radius of $10R_J$ (equivalent to an effective temperature of 1600 K) and a total mass of $6 \times 10^{-3} M_J$ or $1.9 M_{\oplus}$. We also utilized a turbulent broadening equal to 5 times the sound speed. Following the prescription in Dullemond & Dominik (2004), the surface density is given by a split power law with an exponent of -1 out to 0.2 au and -12 from 0.2 to 0.5 au. The steep index in the outer portion effectively provides a “smooth” disk edge at

0.2 au. We chose a scale height ($H/R = 0.2$) at 0.2 au, with H/R scaling as $R^{1/7}$ for a slightly flared disk, and an opacity given by a mix of amorphous and crystalline silicates plus organics.

The model assumes that the gas temperature is coupled to that of the dust, which may not be a good approximation (Kamp & Dullemond 2004). It is possible that the gas is heated above that of the dust through nonthermal heating processes owing to a strong UV field from accretion onto the planet, the central star, or a combination thereof. Higher gas temperatures would result in stronger lines. At the same time, densities may be too low to excite the lines through collisions with atomic and molecular hydrogen, leading to subthermal line populations and weaker overall line intensities (Meijerink et al. 2009). In the RADLite model, such effects are neglected and local thermodynamic equilibrium is assumed. Effectively, the assumptions of coupled gas and dust temperatures with LTE excitation tend to cancel each other out and may produce similar line fluxes to the combined assumptions of decoupled

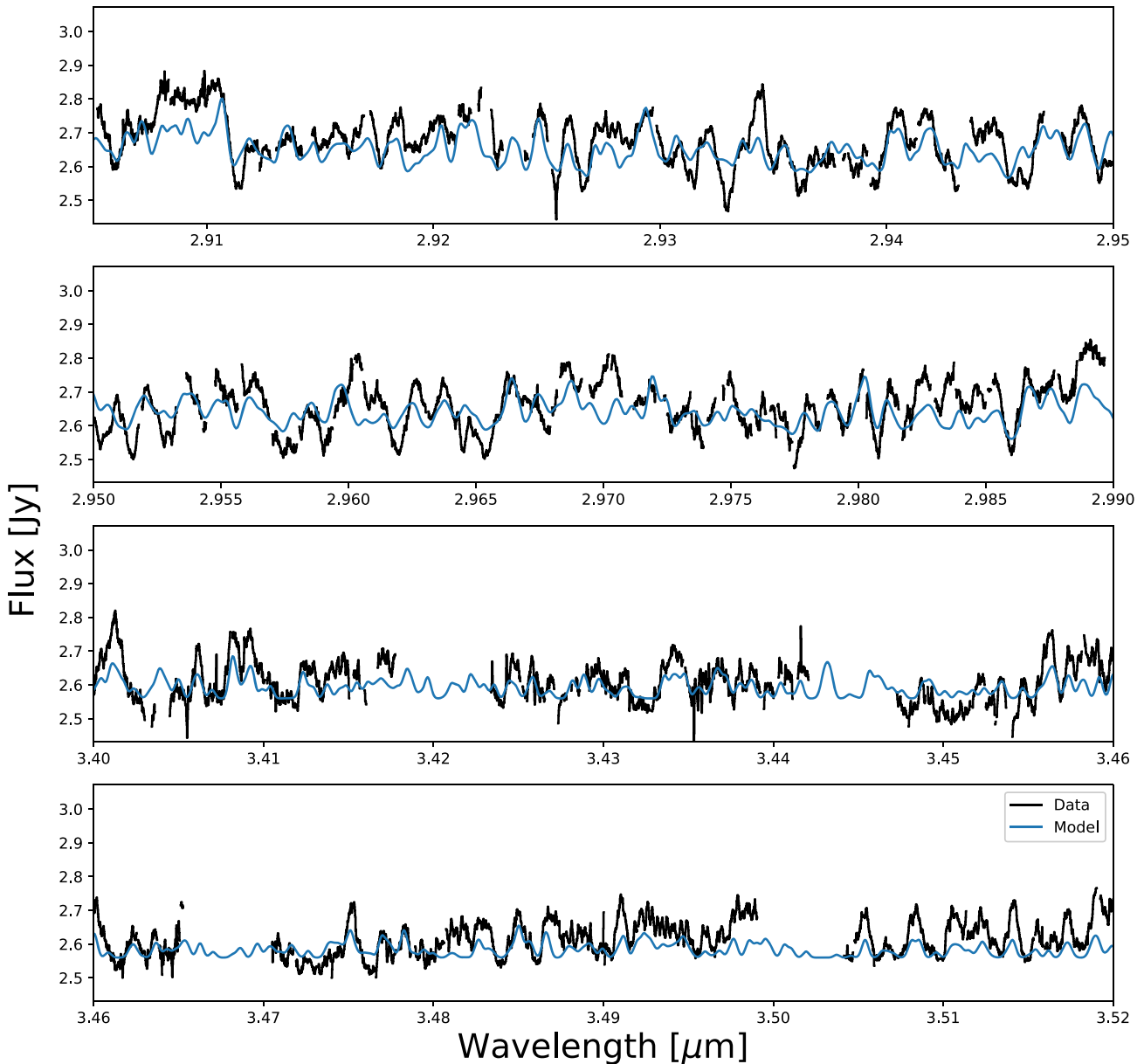


Figure 8. Comparison between a portion of the L -band spectrum of VV CrA A and a RADLite model of a 0.2 au sized disk around a substellar object of mass $6M_J$ and luminosity $0.023 L_\odot$ (see Section 3.4).

gas temperatures plus non-LTE excitation (Meijerink et al. 2009; K. M. Pontoppidan et al. 2022, in preparation). Therefore, the inferred luminosity of the putative planet/substellar companion is plausible, but it is likely associated with a large uncertainty. Similarly, model column densities do not necessarily reflect true column densities.

As shown in Figure 8, our nominal RADLite disk model provides a reasonable match to the data. Although we did not attempt exhaustive model fitting, the disk parameters in our nominal RADLite model—high temperature, gas-to-dust ratio, and turbulent broadening, combined with a very small emitting area, are analogous to the best-fit slab model parameters. Figure 9 shows how the appearance of the spectrum varies with different gas-to-dust ratios. In this figure, all models are scaled to the flux between 2.9292 and 2.9295 μm to investigate the shape of the spectrum, rather than the overall line flux. As the gas-to-dust ratio increases, the line spectrum “flattens out” as

lines with low optical depth rise relative to lines with high optical depth. Water abundance and gas-to-dust ratio can both affect the spectrum in this way and cannot easily be disentangled—the key conclusion that the observable water column must be large is the same as for the slab model.

Figure 10 shows how the line flux in a portion of the spectrum (2.920–2.945 μm) changes as the disk outer radius (more precisely, the power-law break location) is varied; we can see that $\sim 90\%$ of the flux in this wavelength region is contained within 0.05 au of the planet. Therefore, our RADLite modeling also confirms the conclusion that the L -band emission comes from a small region.

In short, we find that it is possible to create a radiative transfer model of a CPD that recreates the observed L -band water spectrum, but the emitting region must be small and hot, with a high gas-to-dust ratio, high water vapor abundance, and high turbulent broadening.

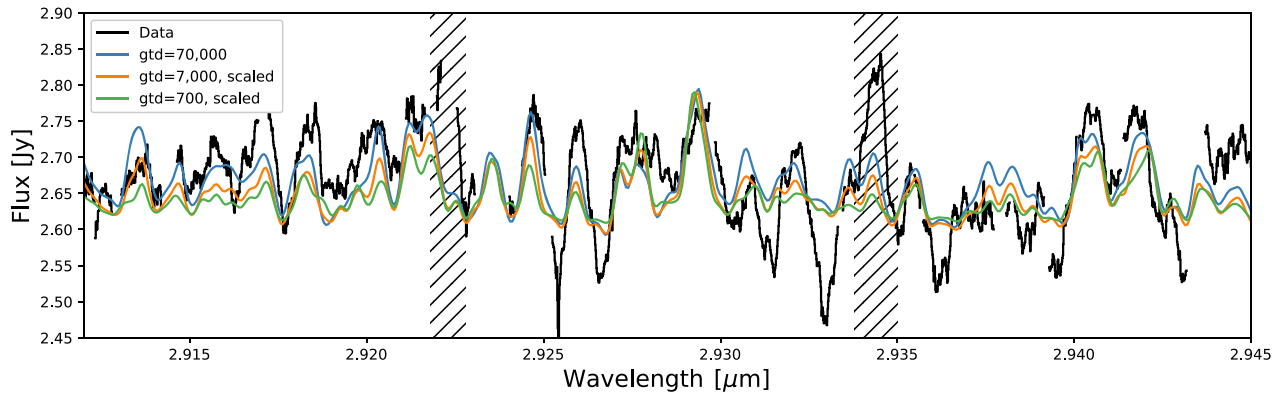


Figure 9. RADLite models with different gas-to-dust ratios, scaled as in Figure 4, compared to data between 2.912 and 2.945 μm . Hatched regions mark OH emission.

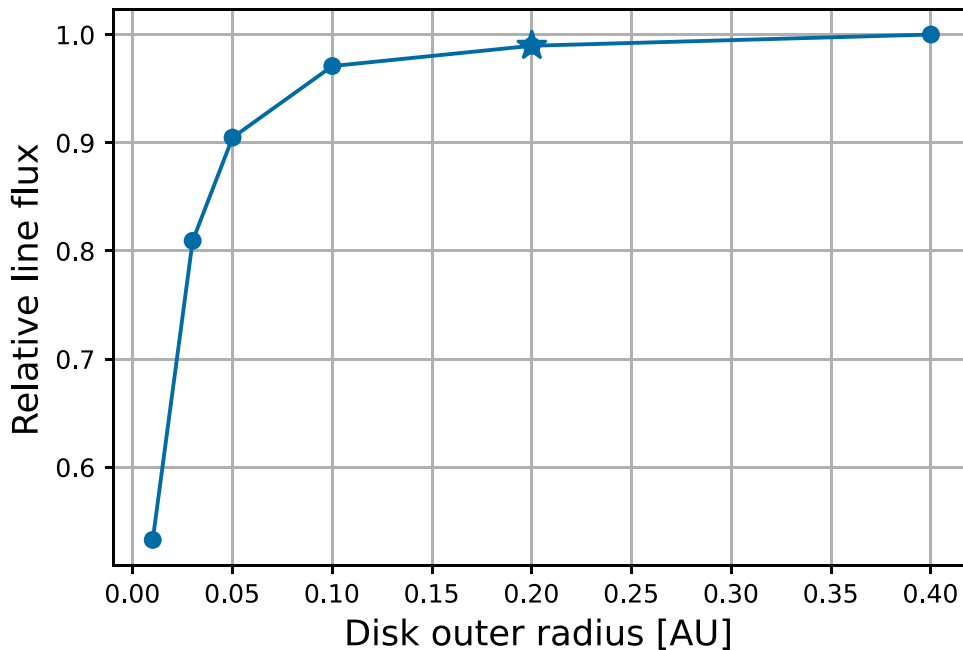


Figure 10. Variation in integrated line flux between 2.920 and 2.945 μm as a function of the disk outer radius. The line flux values are expressed relative to the line flux in the model with $R_{\text{disk}} = 0.4$ au. The star indicates the radius of the nominal RADLite model.

3.5. Constraints from Other Data Sets

3.5.1. Cooler Water Vapor from VV CrA A Observed with Spitzer-IRS and VISIR

Spitzer-IRS spectra of the combined binary system show pure rotational emission from water vapor (Figure 3). The water lines at wavelengths longer than 12 μm appear to be similar to those observed in many other protoplanetary disks, like AS 205, shown for comparison in Figure 3 (Pontoppidan et al. 2010). Since line fluxes rise more rapidly with wavelength for VV CrA than AS 205, the water reservoir for VV CrA may be cooler. Similarly, the high-resolution 12 μm VISIR spectra (Figure 2), which resolve the binary, also show water vapor emission from VV CrA A in several rotational transitions.

These rotational water lines appear to trace a different reservoir of water vapor than the rovibrational lines in the L band. Because of the small emitting area and high temperature of the compact reservoir discussed in Section 3.1, our nominal L -band slab model and our RADLite model produce undetectably small line fluxes in VISIR and Spitzer-IRS observations.

For example, assuming an N -band continuum flux of 20.5 Jy (Sullivan et al. 2019), our nominal L -band slab model predicts a line-to-continuum ratio of $\sim 0.2\%$ for the 12.3757 μm line observed with VISIR, in contrast to the observed ratio of $\sim 10\%$. We show this model in Figure 11. Therefore, the unique water reservoir only appears in the short-wavelength spectra and does not appreciably affect the rotational water lines beyond 12 μm .

Consequently, there must be an additional reservoir of cooler gas in the VV CrA A disk, possibly with larger emitting area and lower column density. Following the analysis described in Salyk et al. (2019), observed ortho/para line flux ratios slightly less than 3 imply that the N -band lines are borderline optically thick and consistent with a column density near 10^{18} cm^{-2} . Furthermore, we find that the data are consistent with a temperature of ~ 1000 K and an emitting area of $\sim 3 \text{ au}^2$, as shown in Figure 11. This model, however, predicts flux in a few L -band emission features 30 times stronger than what we observe. The extrapolation to the L band is highly temperature dependent, however, and lower-temperature models are also consistent with the N -band model to within uncertainties; for

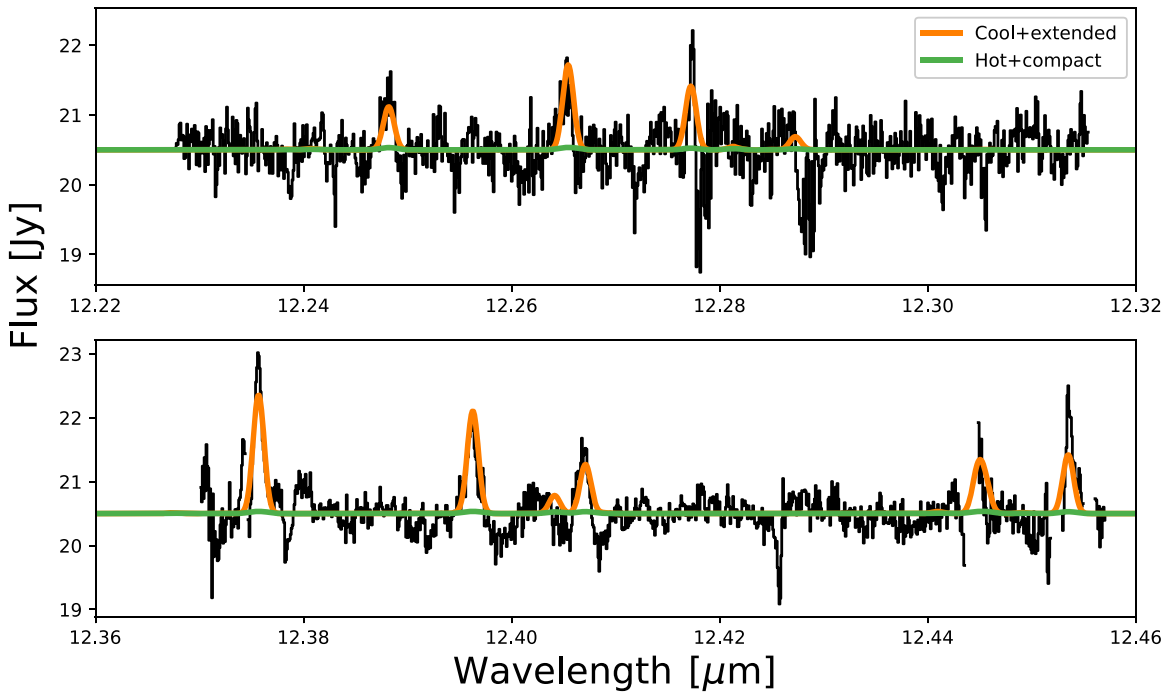


Figure 11. VISIR spectra of VV CrA A in the “OH” and “H₂O” settings, along with two slab models. Green: our nominal *L*-band slab model extended to the *N* band. Orange: a slab model with $T = 1000$ K, $A = 3$ au², and $N_{\text{H}_2\text{O}} = 10^{18}$ cm⁻².

example, a model with $T = 600$ K, $N_{\text{H}_2\text{O}} = 10^{18}$ cm⁻², and $A = 18$ au² can reproduce the *N*-band data and is also consistent with the *L*-band data. There may also be variability in the *L*- or *N*-band emission (e.g., Banzatti et al. 2014, 2015), or variable continuum levels could affect our absolute flux calibration.

As seen in Figure A5, no SA signal is detected in our VISIR data. As discussed in Pontoppidan et al. (2011), the observed SA signal is affected by continuum dilution of the line emission, the effect of which is to make the observed signal smaller than the true line offset. The observed offset is reduced by a factor $(1 + F_c/F_l)$, where F_c is the continuum flux and F_l is the line flux. The strongest upper limit on the spatial extent of the emitting area is therefore usually provided by the emission line with the largest line-to-continuum ratio. The line-to-continuum ratio for VV CrA A in the 12.3757 μm line is 0.11, corresponding to a continuum dilution factor of 10.1. Since the standard deviation of the SA signal is 0.7 au (equivalent to 4 mas), we can constrain the water emission for the 12.3757 μm line to within a radius of $\lesssim 7$ au from the star.

Overall, the VISIR and Spitzer spectra from VV CrA A are consistent with emission from warm ($\lesssim 1000$ K) water vapor in the few au region of the protoplanetary disk. The similarity of the Spitzer (Pontoppidan et al. 2010) and VISIR (Salyk et al. 2019) spectra to other water-rich protoplanetary disks is also consistent with this hypothesis. Therefore, VV CrA A must harbor a cooler ($T \lesssim 1000$ K), larger reservoir of water vapor in addition to the hot ($T \gtrsim 1500$ K), compact reservoir discussed in Section 3.1.

3.5.2. CO Emission and Constraints on the H₂O/CO Ratio

While high water column density is required to fit the *L*-band observations, we do not know whether the spectra arise from a region with high overall gas column or an enhanced H₂O abundance relative to other molecular species. By analyzing the

CO emission in the *K* and *M* bands, it may be possible to distinguish between these two scenarios.

Figure 12 shows the CO *M*-band spectrum for VV CrA A along with a slab model fit to these *M*-band data, found by exploring the same range of temperature, column density, and turbulent broadening as for the *L*-band water emission. We find that the CO *M*-band emission is better fit with a lower temperature ($T \sim 1000$ K) and lower column density ($N_{\text{CO}} \sim 10^{19}$ cm⁻²) than our best fit to the *L*-band water emission. If we instead take our nominal compact, hot *L*-band model, set H₂O:CO = 1, and predict the *M*-band CO emission, we find line fluxes smaller than observed. Therefore, the *M*-band CO data seem to probe a cooler, larger reservoir than the *L*-band data. At the same time, they are fully consistent with the presence of an underlying compact, hot region.

The CRILES *K*-band spectrum (Figure 13) shows a large number of CO overtone ($\nu = 2-0$, $3-1$, and $4-2$) emission features. A CO slab model is shown, in which the emitting area is constrained to be the same as that of the nominal *L*-band model. There are a few water vapor transitions in this region, but it is not entirely clear whether the addition of a water model improves the fit to the data. As an example, we note the mismatch between data and CO model in the 2.383–2.385 μm region, which may indicate the presence of water vapor. The temperature in the CO model is around 2000 K, and column density is very high at $N_{\text{CO}} \sim 5 \times 10^{20}$ cm⁻². However, most lines are optically thin or only marginally optically thick, so the best-fit CO column density is dependent on our assumed emitting area. If it is assumed that the *K*-band CO and *L*-band water probe the same reservoir, this implies a column density ratio of H₂O/CO ~ 0.7 —slightly lower than typical column density ratios of H₂O/CO ~ 1 measured in inner disks (Salyk et al. 2011). However, as we discuss in Section 3.5.3, line shapes suggest that these may not necessarily be probing the same reservoir. As shown in the inset of Figure 13, the *K*-band CO lines are double peaked. In fact, the shape is well fit by the

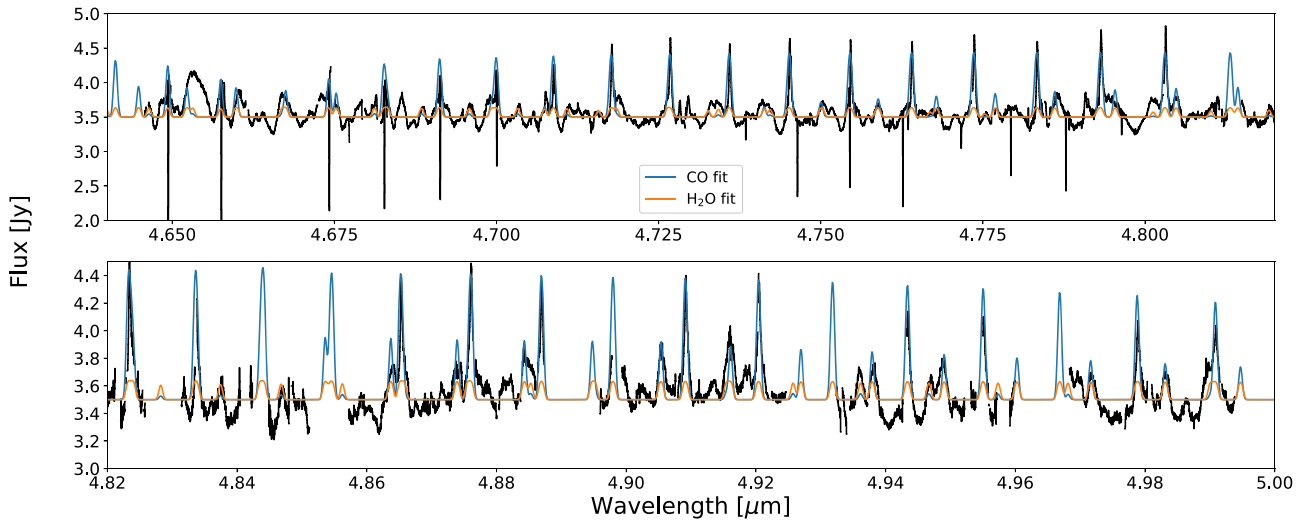


Figure 12. *M*-band CRIRES spectrum of VV CrA A with best-fitting CO slab model ($T = 1000$ K, $N_{\text{CO}} = 1 \times 10^{19}$ cm $^{-2}$, $v = 10$ km s $^{-1}$, and $A = 0.06$ au 2 ; blue) and a model with the same parameters as our nominal *L*-band model ($T = 1500$ K, $N_{\text{CO}} = 3 \times 10^{20}$ cm $^{-2}$, $v = 10$ km s $^{-1}$, and $A = 0.003$ au 2 ; orange), assuming $\text{H}_2\text{O}:\text{CO} = 1$.

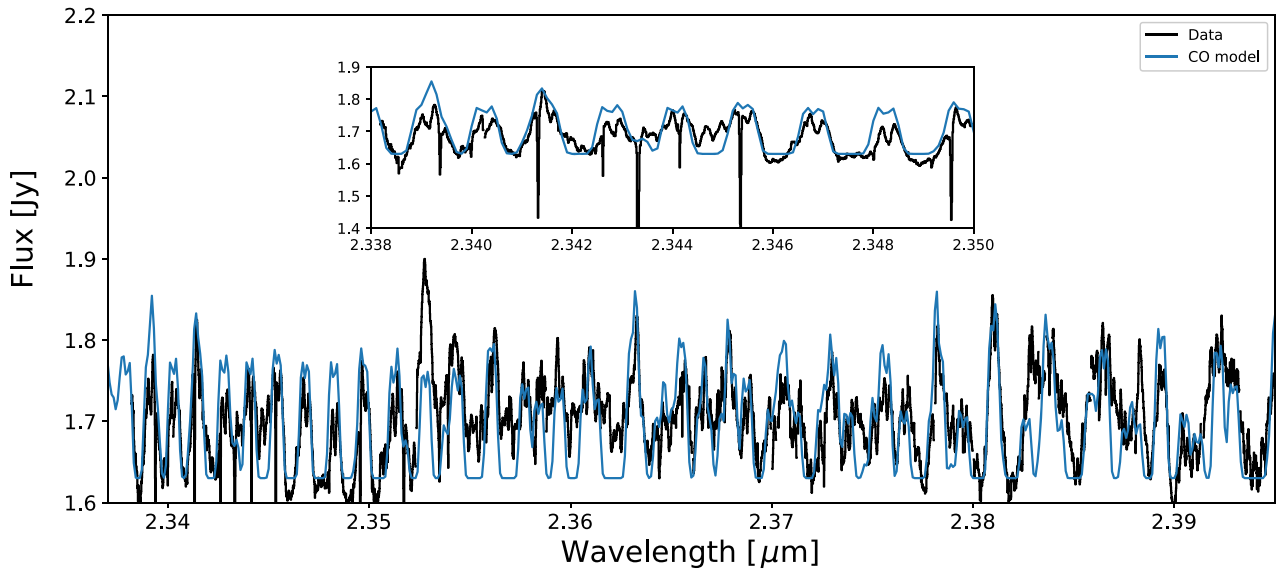


Figure 13. CRIRES *K*-band spectrum of VV CrA A (black) and a slab model convolved with the inner disk line profile (Figure 7, left panel) discussed in Section 3.3 (blue). The inset highlights the double-peaked line profiles.

inner disk ring model discussed in Section 3.3, which is located at the dust inner radius of 0.17 au.

3.5.3. Velocity Information

Emission lines from each wavelength regime appear to have distinct line shapes, suggesting that they each probe different reservoirs. We show a compendium of line shapes in Figure 14. The CO *K*-band spectrum is double peaked, with peak locations near 28 km s $^{-1}$ —similar to the inner disk model shown in Figure 7. VISIR and CO *M*-band lines appear Lorentzian in shape, with *M*-band lines being broader. It is not possible to extract an isolated H $_2$ O line from the *L*-band spectrum, so we show here our wide ring model (middle panel of Figure 7). This particular model appears intermediate in width between the *K*- and *M*-band lines, although it is not uniquely specified by the *L*-band data; the CPD model, for example, is narrower than the *M*-band line shape.

A simple understanding of protoplanetary disks would predict narrowing of line profiles as observations probe longer wavelengths (i.e., as one probes from the *K* to the *N* bands), although it should be kept in mind that emission lines at similar wavelengths may probe a variety of excitation levels (see, e.g., Figure 5). The *K*-, *M*-, and *N*-band data follow this trend, narrowing with increasing wavelength, and the *K*-band data appear well described with a line shape produced at the dust inner rim (Figure 13). Non-Keplerian motion is likely required to explain the Lorentzian-like *M*- and *N*-band profiles (e.g., Bast et al. 2011). Lorentzian-like *M*-band CO rovibrational emission has previously been attributed to the presence of low-velocity disk winds (Pontoppidan et al. 2011; Banzatti et al. 2022). A contribution from a CPD would also cause deviations from the simple disk velocity trend, but we cannot say definitively how the *L*-band emission-line profile compares to other wavelengths.

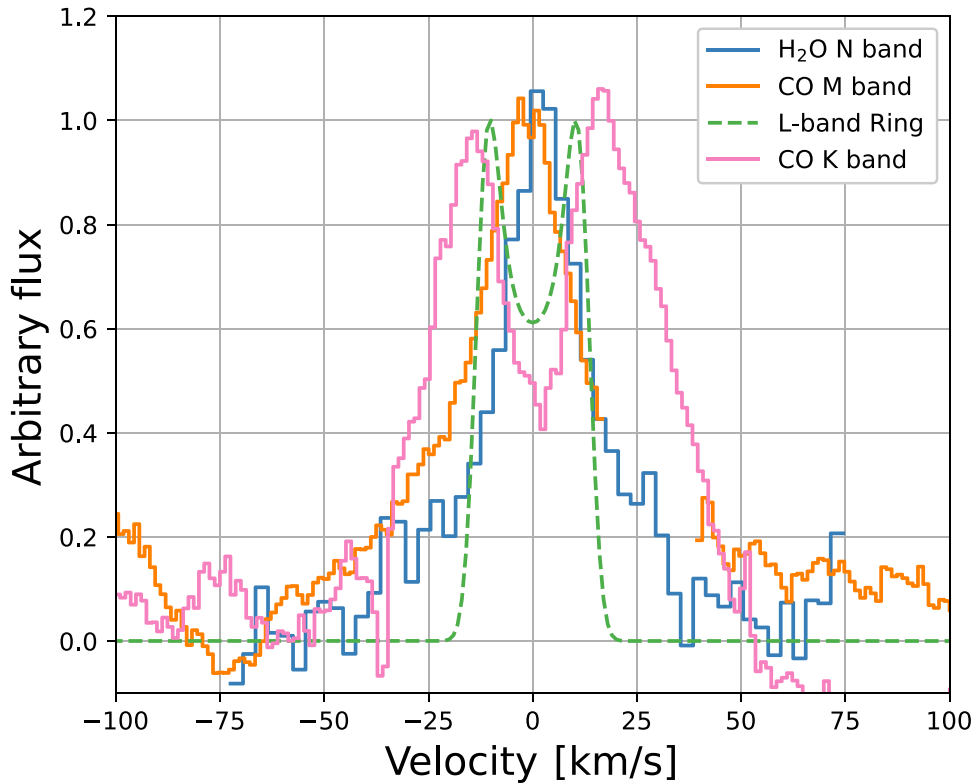


Figure 14. A comparison of observed line shapes: VISIR water vapor line composite (blue), CO M band ($v = 1-0 P(22)$; orange), CO K band ($v = 3-1 R(15)$; pink), and our L -band wide ring model (green dashed—see Section 3.3). Velocities are stellocentric, assuming a stellar velocity of -1 km s^{-1} (Fang et al. 2018).

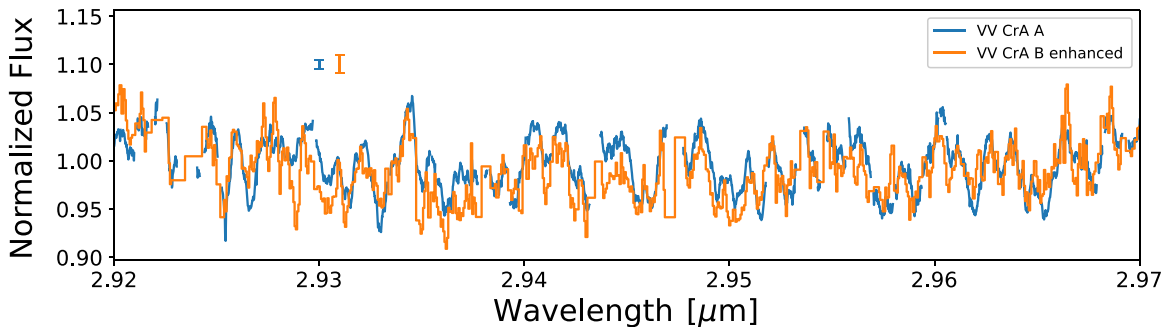


Figure 15. Comparison between portions of the L -band spectrum of VV CrA A and an enhanced spectrum of VV CrA B (see text for details). Representative error bars (assumed to be $3\times$ the statistical error) are shown in the upper left corner.

The plot also shows that emission velocities all appear close to the stellar velocity. Although in this plot the M -band CO appears shifted by $\sim 3 \text{ km s}^{-1}$, analysis of a suite of emission lines suggests no statistically significant shift, with a systematic uncertainty of a few kilometers per second. Similar uncertainties of a few kilometers per second are found for the K - and N -band lines. In short, we find no statistically significant deviations of any velocities from the systemic velocity.

3.6. VV CrA B

The L -band spectrum of VV CrA B has a lower S/N and lower line/continuum ratios than the spectrum of VV CrA but shows some of the same features. In Figure 15, we show a comparison between the VV CrA A spectrum and the spectrum of VV CrA B modified in two ways—it has been binned by a factor of 5, and then it had its line/continuum ratio enhanced by a factor of 3. With these enhancements, there is a strong

correspondence between the shapes of two spectra—the data sets shown in this figure have a Pearson R coefficient of 0.96.

The M -band spectra from CRILES (Figure 1) reveal primarily deep CO absorption lines from VV CrA B, as discussed in Smith et al. (2009), although three CO $v = 2 - 1$ lines are detected in emission—see Figure 16. A comparison of the emission from the two stars in the same transitions shown in Figure 16 reveals similar emission-line shapes for the two disks, suggesting similar CO-emitting locations and disk inclinations. A slight velocity offset is observed, but the S/N of the VV CrA B data is too low to make this result significant.

There is a marginal detection of water vapor in VV CrA B at $12.3757 \mu\text{m}$ in the combined H₂O VISIR setting (Figure 17) and at multiple transitions for the 2017 September 08 data alone (Figure A5). The difference in the water line-to-continuum ratio for the two disks could arise from differences in excitation conditions (temperature, density, etc.), different water abundances, or different inclination angles. However, the

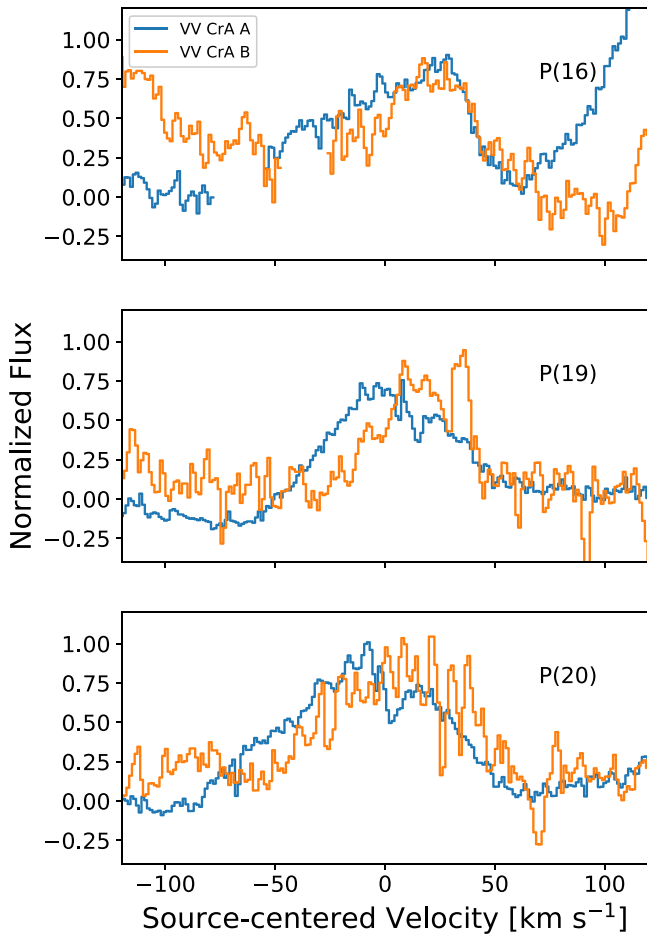


Figure 16. Normalized CO $\nu = 2-1$ emission from VV CrA A (blue) and VV CrA B (orange).

similarity of the CO emission-line shapes in the two disks argues against different inclinations.

In short, the spectra of VV CrA B suggest that similar reservoirs of water vapor and CO exist in the disks around VV CrA A and B, albeit with some difference causing a lower line/continuum ratio for B. Higher-S/N data would be useful to confirm this result. The similar CO emission-line shapes for the two disks also support a scenario in which the CO absorption seen toward VV CrA B is caused by foreground absorption by VV CrA A, rather than self-absorption in an inclined disk around VV CrA B.

4. Discussion

4.1. Correlation with Evolutionary State

To our knowledge, the complex L -band spectral patterns we present in this work have only been seen in one prior study, that of V1331 Cyg (Doppmann et al. 2011). A possible reason for this rarity may be that most of the high-resolution L -band spectroscopic studies have focused on later evolutionary states (Salyk et al. 2008; Mandell et al. 2012; Banzatti et al. 2017). The age of VV CrA is somewhat uncertain, with estimates ranging from a fraction of a Myr (Prato & Simon 1997) to several Myr (Scicluna et al. 2016). But the accretion rate of VV CrA A ($3 \times 10^{-7} M_{\odot} \text{ yr}^{-1}$; Fang et al. 2018) is higher than that of typical T Tauri stars, and it is associated with a Herbig-Haro object (Wang et al. 2004), indicative of an outflow. The

presence of similar water emission features in the coeval disks around VV CrA A and B is also consistent with this reservoir correlating with evolutionary state.

The presence of CO overtone emission from VV CrA A also makes it an atypical T Tauri star. CO overtone emission is more commonly observed around hotter (especially B-type) Herbig stars (Ilee et al. 2014). It has been detected from some T Tauri stars as well, but it is associated with outflows (Carr 1989). Given the high temperatures required to excite the CO overtone lines, their presence from a T Tauri star may require an accretion burst to provide additional localized heating (Ilee et al. 2014). The strongly single-peaked emission lines observed from VV CrA A in the M band are also associated with low-velocity molecular disk winds (Bast et al. 2011; Pontoppidan et al. 2011; K. M. Pontoppidan et al. 2022, in preparation), which may be stronger when the star is more actively accreting.

A similar reservoir of both CO and water with high gas column densities, high temperatures, and high turbulent velocities was observed around SVS 13 (Carr et al. 2004), a young binary system (Diaz-Rodriguez et al. 2022) in NGC 1333 (Strom et al. 1976). SVS 13 is a Class I young stellar object (Bitner et al. 2008) with higher-than-average accretion ($6 \times 10^{-7} M_{\odot} \text{ yr}^{-1}$; Edwards et al. 2003) and both outflow and wind signatures (e.g., Edwards et al. 2003; Diaz-Rodriguez et al. 2022). Unfortunately, no direct comparison can be made with our spectra because the two sources were not observed at the same wavelengths.

A direct comparison can, however, be made with an L -band spectrum of V1331 Cyg, presented by Doppmann et al. (2011). Similar to our work, they show that the many water features in the V1331 Cyg spectrum have similar line strengths, requiring a high column density. They report best-fit water model parameters similar to ours— $T = 1500$ K, $N_{\text{H}_2\text{O}} = 2 \times 10^{21} \text{ cm}^{-2}$, and $A = 0.02 \text{ au}^2$ —albeit with somewhat larger water vapor column density and emitting area and no additional turbulent broadening. V1331 Cyg is a young A8–G5 star in L988, with an accretion rate $> 3 \times 10^{-7} M_{\odot} \text{ yr}^{-1}$ (see Doppmann et al. 2011, and references therein).

Does a correlation with evolutionary state, and with the presence of outflows and/or winds, help constrain the physical origin of the emission? We might expect these properties to be associated with high inner disk gas temperatures and turbulent velocities, just as observed in the L -band data. In addition, it is plausible that a high accretion luminosity could push dust sublimation outward, while water self-shielding (Bethell & Bergin 2009) maintains a region of high water abundance close to the star; in combination, this could produce a region with high observable water columns, as seen in our L -band data. In short, VV CrA’s evolutionary state provides plausible ways to produce conditions in the inner disk consistent with those seen in the L -band data.

As discussed in Section 3.3, there is not a good match between observed and predicted line shapes for an inner disk model. However, given VV CrA’s evolutionary state and single-peaked CO emission lines, it is likely that it has a molecular wind (e.g., Bast et al. 2011; Pontoppidan et al. 2011; Banzatti et al. 2022). Perhaps the non-Keplerian motions in this wind could alter water line shapes sufficiently to reconcile the observed spectral shape with gas located close to the dust inner rim (i.e., the inner ring model of Figure 7). In other words, the emission could arise not only from the disk itself but also from

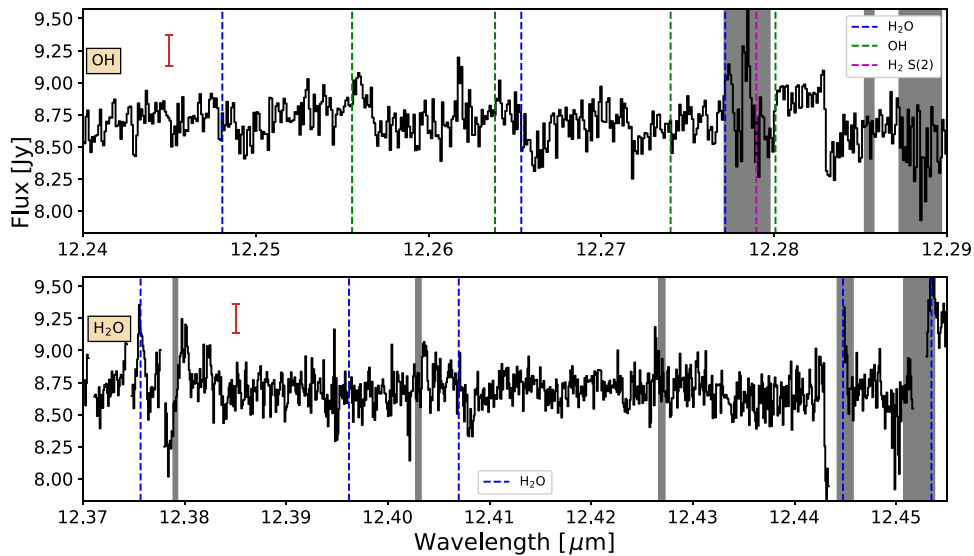


Figure 17. Reduced spectra of VV CrA B in the two water/OH settings observed with VISIR. Data wavelengths are heliocentric, and theoretical wavelengths have been shifted by -21 km s^{-1} , the velocity of CO $v = 2 - 1$ emission from VV CrA B. In the upper left corner, we show representative error bars computed from the standard deviation of flat spectral regions.

the base of the molecular wind. A higher velocity or extended outflow origin, however, appears inconsistent with the low (same as systemic) line-center velocities and small spatial extent of the emission.

As for the CPD hypothesis, the fact that the observed hot water reservoir appears to be associated with early evolutionary states would imply that the CPD must be easier to detect in early stages than later stages of disk evolution. This could naturally be explained by a reduction in planetary luminosity and/or CPD viscous heating with time, or by changes in H_2O abundances (e.g., Ilee et al. 2017) and temperatures (e.g., Canup & Ward 2002) with time that could potentially create distinct observability windows. In addition, the models of Marley et al. (2007) predict a rise in planetary luminosity during a brief period between 2 and 3 Myr.

It may be argued that if CPDs are rare, it would be unlikely for one to detect similar signatures from both VV CrA A and B. However, dynamical signatures of protoplanets are being detected in a majority of bright disks observed with ALMA at high resolution (e.g., Andrews et al. 2018; Pinte et al. 2020), and binarity only appears to affect planetary occurrence rates for small separations (e.g., Kraus et al. 2016). Therefore, it may be reasonable for CPDs to exist in both disks of the binary pair.

4.2. Is Our CPD Model Realistic?

Is our RADLite model in Section 3.4 a realistic model of a CPD? We have very few observational constraints on CPD properties, but we can compare to the observed disk around PDS 70 c (Isella et al. 2019), and existing CPD models. The PDS 70 c CPD has a dust mass between 2×10^{-3} and 4.2×10^{-3} ; the gas mass is unconstrained. Our model’s high gas-to-dust ratio of 70,000 implies a dust mass of only $2.7 \times 10^{-5} M_{\oplus}$ —significantly lower than that of PDS 70c’s CPD. In addition, our model disk size is 0.2 au, while that of PDS 70c’s CPD is estimated to be between 1.4 and 3 au. However, models suggest that CPD size should be proportional to the Hill radius (e.g., Quillen & Trilling 1998; Ayliffe & Bate 2009) and thus semimajor axis. Therefore, our model disk

could correspond to a CPD 7–15 times closer than the 35 au orbital radius of PDS 70 c, i.e., a disk at 2.3–5 au. A smaller CPD might also have a lower overall dust mass, again, consistent with our model. In addition, as shown in Figure 10, our model is not sensitive to emission beyond ~ 0.05 au, so a larger disk would also be consistent with the observed spectrum.

PDS 70 c is estimated to have a mass between $4M_J$ and $12M_J$, consistent with our modeled planet mass of $6M_J$. However, the luminosity of PDS 70 c is estimated to be $\sim 6 \times 10^{-5} L_{\odot}$, while our model planet has a significantly higher luminosity of $0.02 L_{\odot}$. Our model essentially requires a high luminosity to produce the strong observed water line fluxes, as the model assumes that the disk is passively heated. While different from PDS 70c’s luminosity, our model’s luminosity is fully consistent with core accretion evolutionary tracks in which the planetary luminosity rises higher than $0.02 L_{\odot}$ during runaway gas accretion (Marley et al. 2007). As an alternative to passive heating from the central planet, the CPD might also be actively heated by accretion from within the disk itself. This could be consistent with the high turbulent broadening required to match the observed spectra. Indeed, models predict temperatures consistent with those we observe (e.g., Ayliffe & Bate 2009; Zhu 2015) in at least parts of the CPD. In addition, models predict enhanced H_2O abundances, as the high temperatures cause sublimation of icy grains (e.g., Ayliffe & Bate 2009; Ilee et al. 2017).

We might also compare to the solar system’s Galilean satellites. Our modeled water emitting area is 0.003 au^2 , while a disk extending to Callisto’s semimajor axis would have an area about a factor of 6 smaller— $5 \times 10^{-4} \text{ au}^2$. As discussed in Canup & Ward (2002), the planetary accretion can potentially raise local temperatures several thousands of degrees. In addition, the formation of the Galilean satellites may have required a continual enhancement of metallicity in the inner disk; these solids would sublime at high temperatures, potentially resulting in a disk with enhanced water-to-dust ratios at some stages of the disk’s evolution. The high water

column density seen in our L -band spectra could arise from such a water abundance enhancement.

4.3. Distinguishing between Models

How might we use future observations to better understand the origin of the L -band water emission? It would be helpful to better understand the occurrence rate of this phenomenon and, especially, whether its occurrence correlates with evolutionary state or any other disk properties. SA data in the M and L bands would also be helpful for characterizing any contributions to the emission from a molecular wind (Pontoppidan et al. 2011). If present in many young disks, and if no ancillary data support the existence of a CPD, it will be necessary to reconcile the observed line kinematics with our expectations for protoplanetary disks.

On the other hand, a CPD might have additional detectable signatures. It has been predicted for some time that CPDs would produce both asymmetries and variability in near-IR CO emission lines (Regály et al. 2014). Time variations and asymmetries have been seen in the spectra of the disk around HD 100546 along with variable SA signatures, and Brittain et al. (2014) argue that these are consistent with the presence of a CPD. Spectro-astrometry might be performed for VV CrA A in the L band, although with line-to-continuum ratios of 5%–10% for the water lines, it suffers from continuum dilution factors of 11–21. With an SA rms of 5 mas, one can detect separations of 8–16 au. The CPD would also have a central velocity that differs from that of the star and varies throughout the planet’s orbit. The CPD’s speed should be resolvable with CRILES but would require understanding and accounting for systematic uncertainties in our velocity measurements. If the planet is at 2.3–5 au, we would expect velocities of roughly a few kilometers per second, varying with a period of 4.7–15 yr. A spatial offset for the hot water lines could also be directly measured with an instrument like JWST’s NIRSpec IFU, but unfortunately VV CrA A’s brightness is above NIRSpec’s saturation limits.

A CPD could also be searched for via direct imaging of its millimeter-wave emission (e.g., Zhu et al. 2018) or accretion signatures (Sallum et al. 2015), although its detectability would depend on its angular separation from the star. Published millimeter-wave images (Sciicluna et al. 2016) have a beam size of $1''$ – $2''$, equivalent to ~ 150 – 300 au at 157 pc, hence insufficient to detect a close-in embedded planet. Spectral energy distributions can also indicate large gaps, but the VV CrA disks are heavily embedded, impeding detections of any gaps (Kruger et al. 2011; Sciicluna et al. 2016; Sullivan et al. 2019).

Flipping this discussion on its head, this investigation suggests that it is at least plausible that expected CPD properties would produce a detectable L -band water emission signature. Therefore, it would be worthwhile to couple hydrodynamic CPD models with radiative transfer to make

more realistic predictions for the L band. This could potentially provide a new avenue for discovering CPDs.

5. Conclusions

In this work, we have presented spectra of the VV CrA binary observed with VLT-CRILES, VLT-VISIR, and Spitzer-IRS. We find that the VV CrA A disk presents a water emission spectrum at mid-IR wavelengths that is typical for T Tauri stars; in contrast, in the L band, the spectrum contains an unusual number of high-temperature lines with similar line strengths. Using both slab models and the LTE disk modeling code RADLite, we show that producing such a spectrum requires a small reservoir of hot gas with a large water vapor column density and high turbulent broadening. Line kinematics do not match well with a model in which the L -band emission arises from just outside the dust inner rim in a Keplerian disk. Since the presence of this reservoir is seemingly linked to the presence of high accretion rates and winds/outflows, non-Keplerian motion may be required to explain the emission. We also show that a compact spot, such as a CPD, may provide emission features consistent with those observed. Additional exploration of this phenomenon in other targets, exploration of variability and asymmetry of the molecular emission from VV CrA, and ancillary data to search for any possible CPD signatures are warranted to better understand the physical origin of this unusual spectral pattern.

C.S. would like to thank all who assisted with the planning and observations in the VISIR large program, including the support staff at the VLT. C.S. would also like to acknowledge helpful comments on this work from Michael R. Meyer and Greg Doppmann. C.H. is a former Winton Fellow, and this research has been supported by Winton Philanthropies / The David and Claudia Harding Foundation. C.H. received funding from the European Union’s Horizon 2020 research and innovation program under the Marie Skłodowska-Curie grant agreement No. 823823 (RISE DUSTBUSTERS project). C.H. and R.A. acknowledge support from the European Research Council (ERC) under the European Union’s Horizon 2020 research and innovation program (grant agreement No. 681601). A.C. acknowledges funding from ANR of France under contract No. ANR18CE310019 (SPLASH). This work is supported by the French National Research Agency in the framework of the Investissements d’Avenir program (ANR-15-IDEX-02), through the funding of the “Origin of Life” project of the Grenoble-Alpes University.

Appendix Complete Reduced Spectra

Figures A1–A4 show complete CRILES spectra of VV CrA in the K , L , and M bands, along with our nominal RADLite CPD model. Figure A5 shows our VISIR SA data.

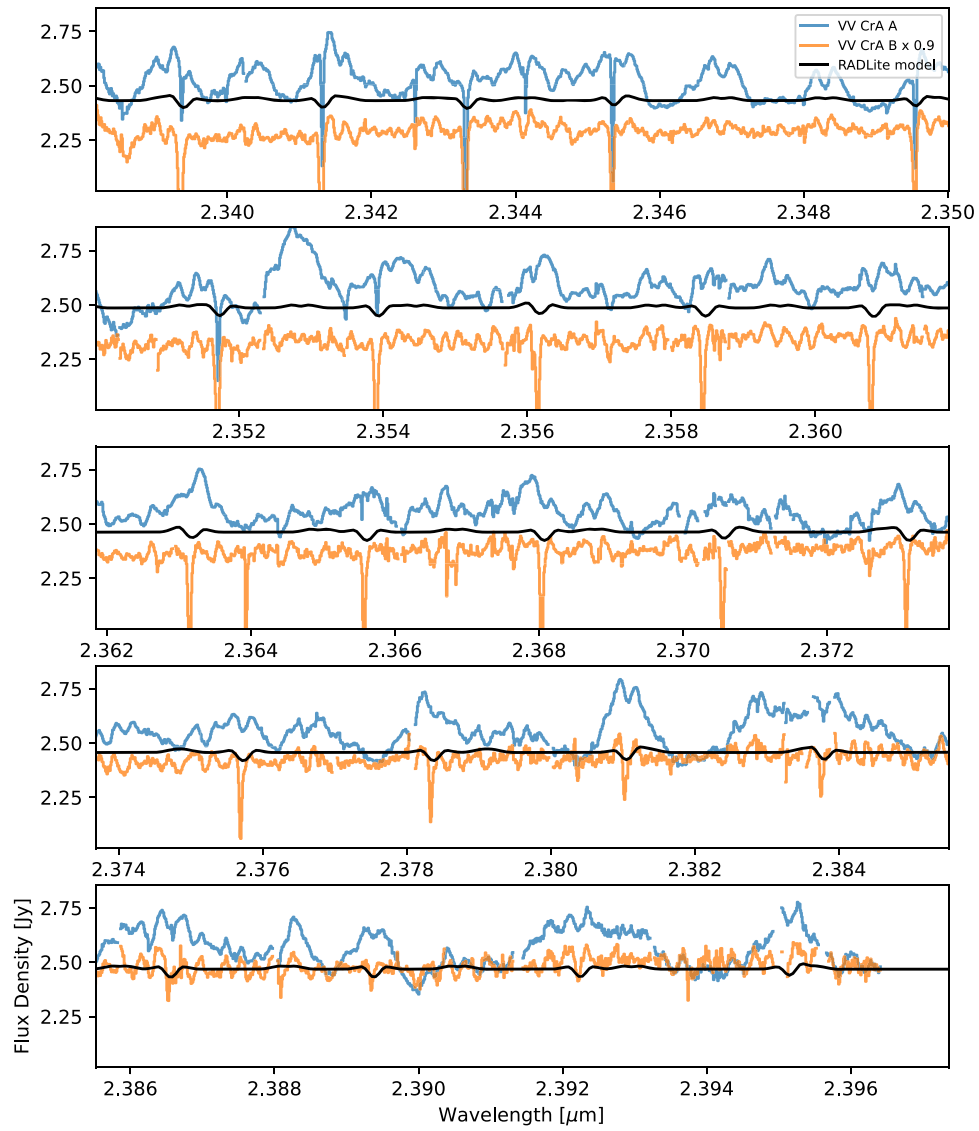


Figure A1. Reduced CRIREs spectra of VV CrA A (blue) and B (orange) in the *K* band. In this and Figures A2–A4, the black curve shows our nominal *L*-band RADLite model.

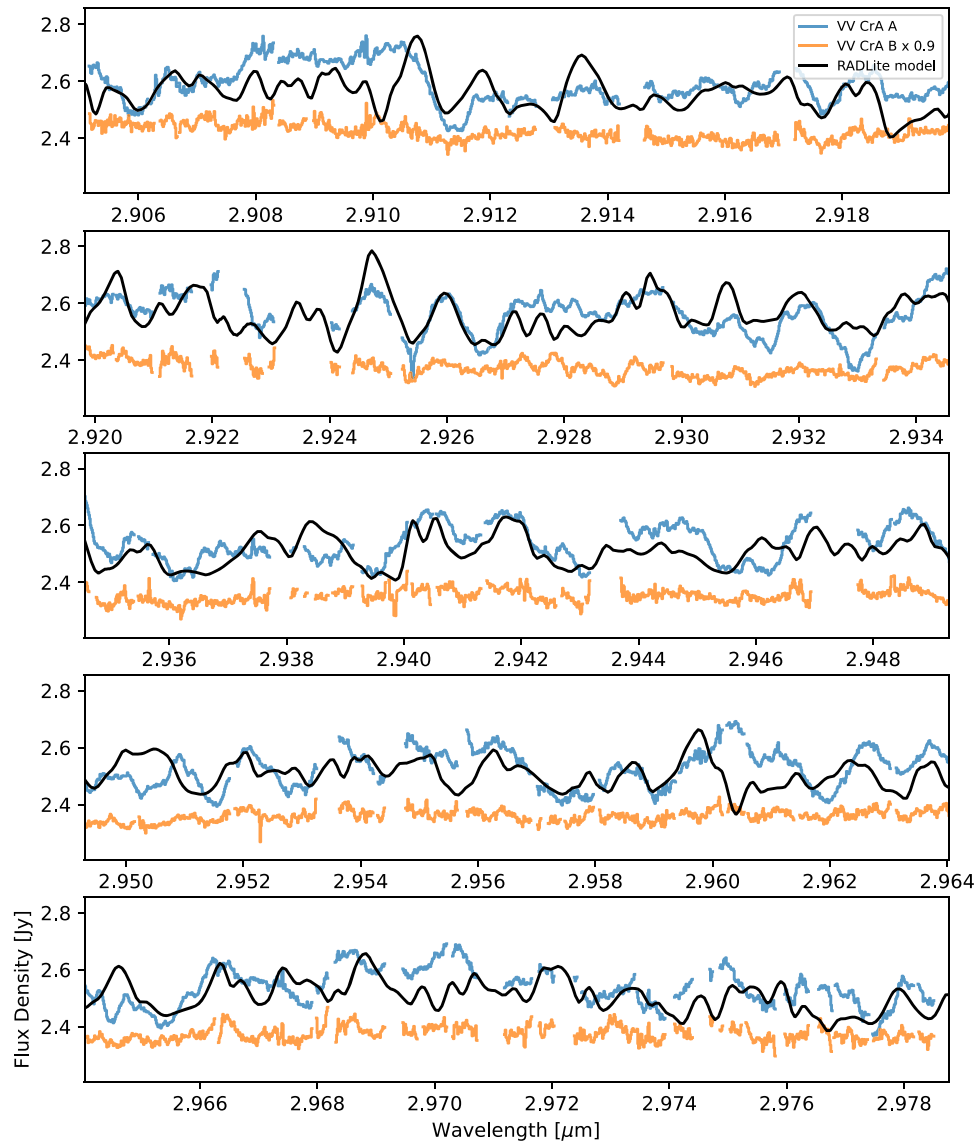


Figure A2. Reduced CRIRCS spectra of VV CrA A and B in the *L*-band “H₂O” setting.

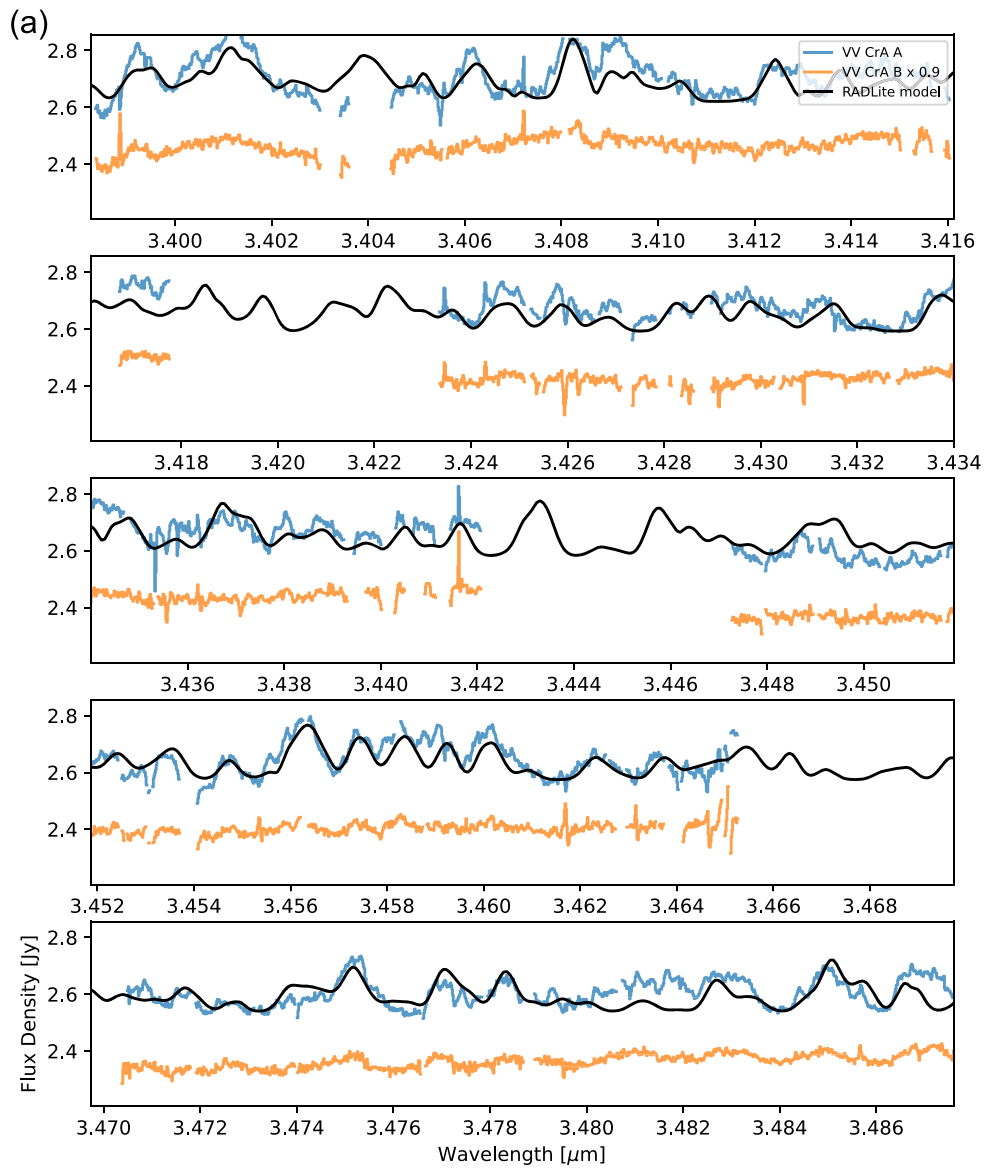


Figure A3. (a) First part of reduced CRIRES spectra of VV CrA A and B in the L -band “organics” setting. (b) Second part of reduced CRIRES spectra of VV CrA A and B in the L -band “organics” setting. (c) Third part of reduced CRIRES spectra of VV CrA A and B in the L -band “organics” setting. (d) Fourth part of reduced CRIRES spectra of VV CrA A and B in the L -band “organics” setting. The broad emission line at $3.741 \mu\text{m}$ is H I Pf $_{\gamma}$.

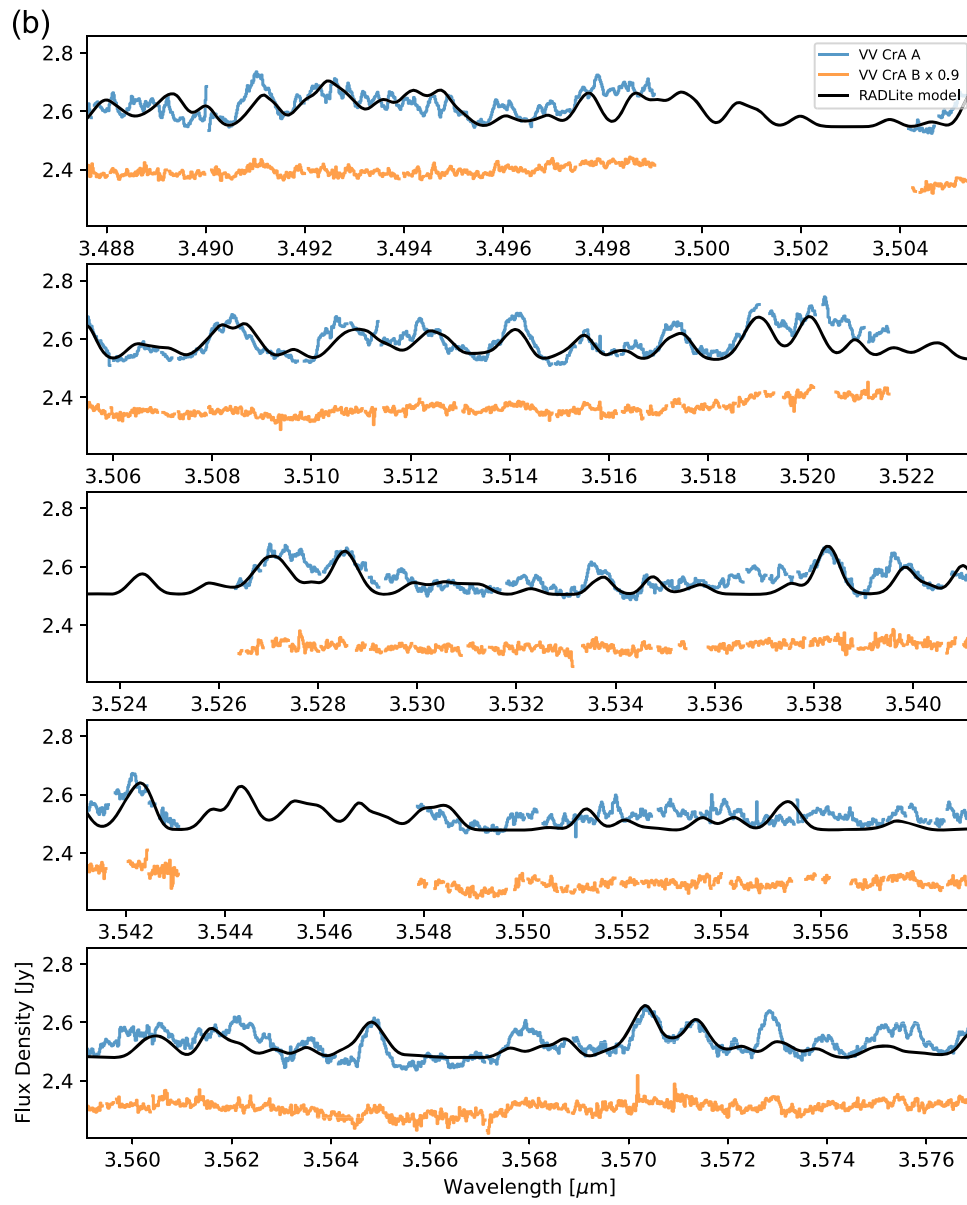


Figure A3. (Continued.)

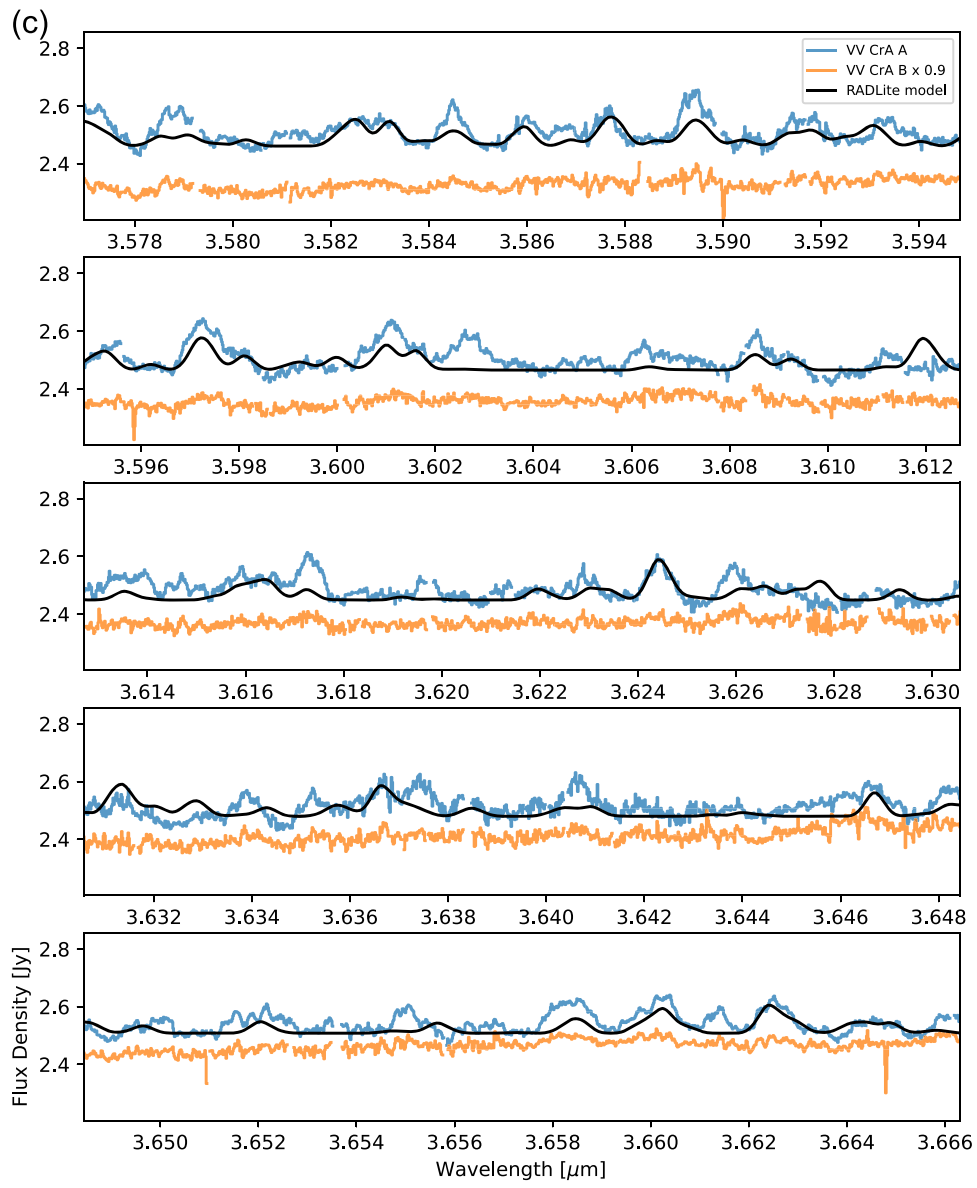


Figure A3. (Continued.)

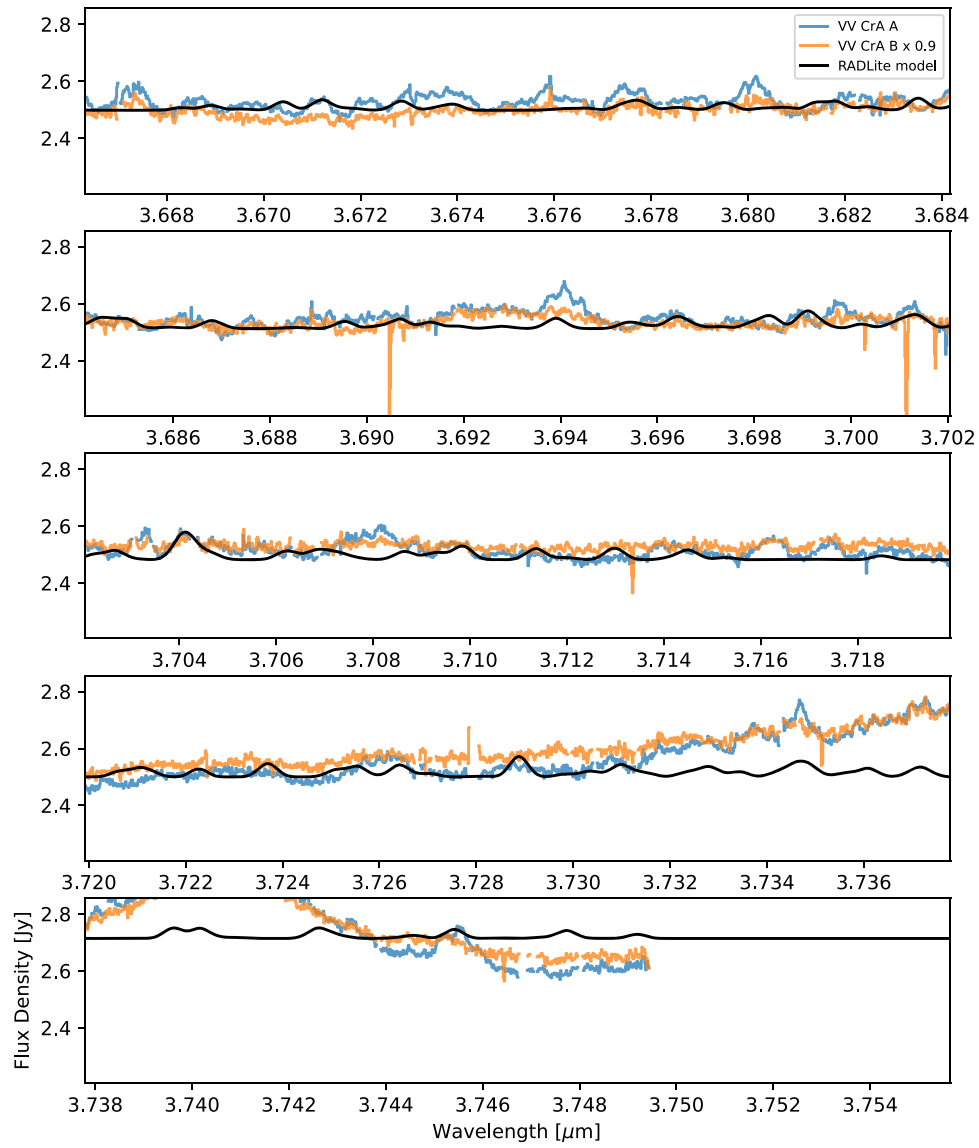


Figure A3. (Continued.)

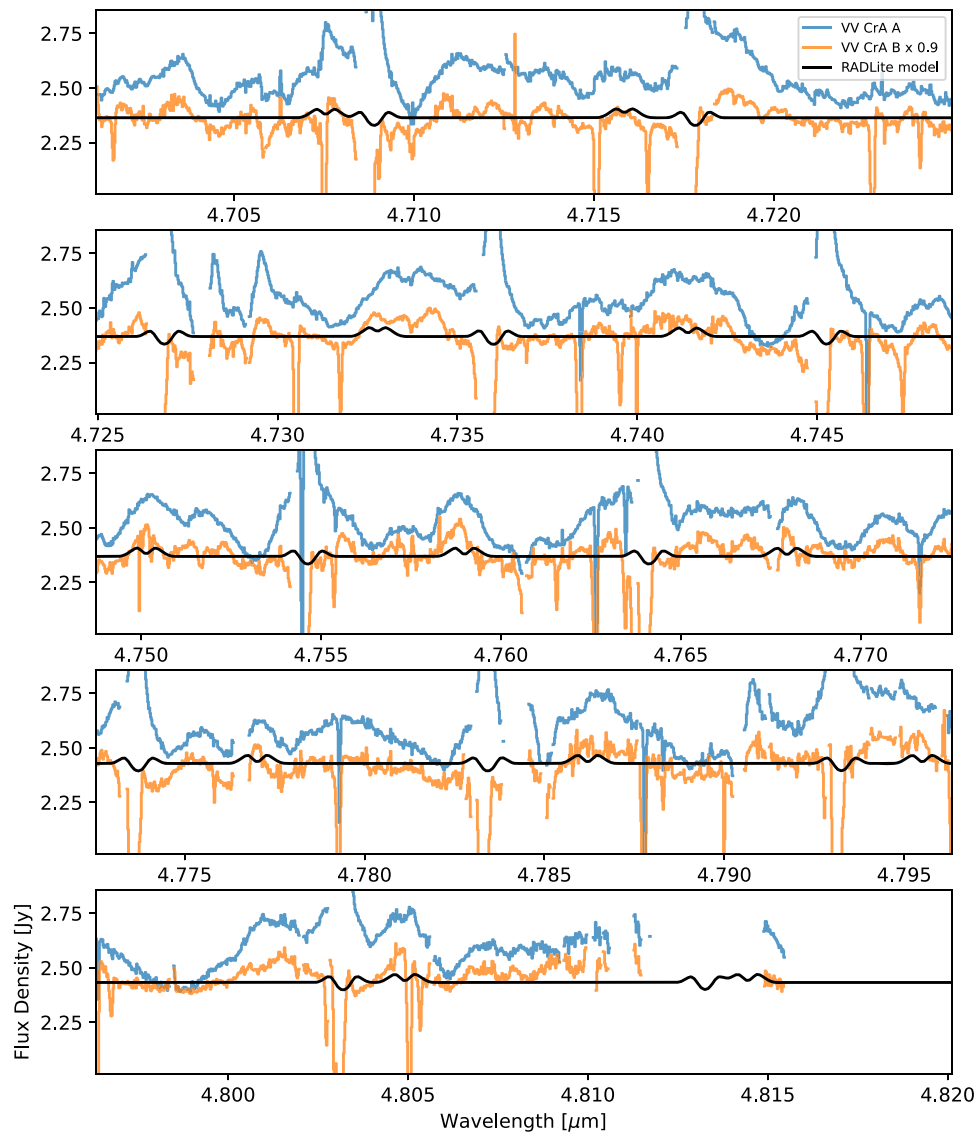


Figure A4. Reduced CRiRES spectra of VV CrA A and B in the *M* band.

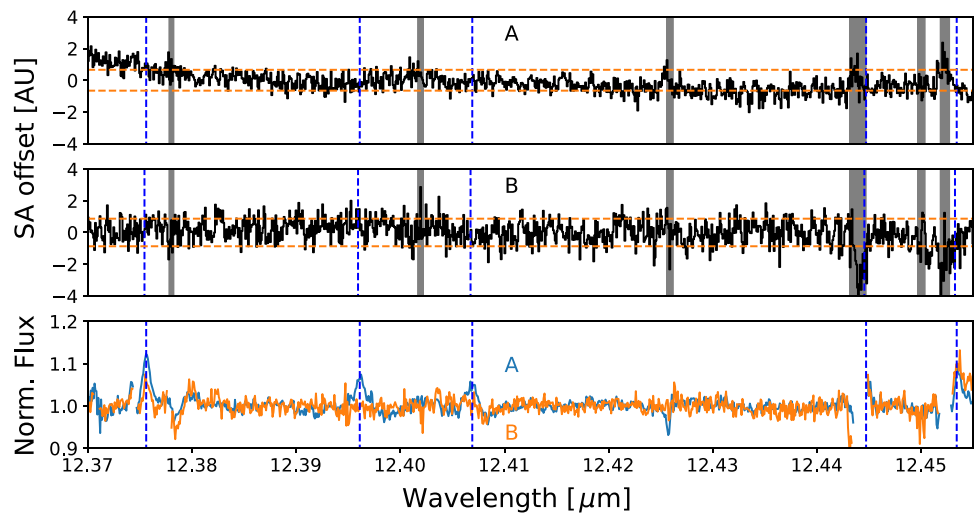












Figure A5. Top two panels: SA measurement in the 12.414 μm water setting for VV CrA A (top) and B (middle). Dashed horizontal lines mark plus and minus one standard deviation. Dashed vertical lines mark theoretical locations of water transitions. Bottom panel: the reduced spectra for VV CrA A (blue) and B (orange), for reference.

ORCID iDs

Colette Salyk  <https://orcid.org/0000-0003-3682-6632>
 Klaus M. Pontoppidan  <https://orcid.org/0000-0001-7552-1562>
 Andrea Banzatti  <https://orcid.org/0000-0003-4335-0900>
 Ulrich Käufel  <https://orcid.org/0000-0002-8806-9795>
 Cassandra Hall  <https://orcid.org/0000-0002-8138-0425>
 Ilaria Pascucci  <https://orcid.org/0000-0001-7962-1683>
 Andrés Carmona  <https://orcid.org/0000-0003-2471-1299>
 Geoffrey A. Blake  <https://orcid.org/0000-0003-0787-1610>
 Richard Alexander  <https://orcid.org/0000-0001-6410-2899>
 Inga Kamp  <https://orcid.org/0000-0001-7455-5349>

References

- Andrews, S. M., Huang, J., Pérez, L. M., et al. 2018, *ApJL*, 869, L41
 Avilez, I., Prato, L. A., Allen, T., et al. 2017, AAS Meeting, 229, 241.04
 Ayliffe, B. A., & Bate, M. R. 2009, *MNRAS*, 397, 657
 Banzatti, A., Abernathy, K. M., Brittain, S., et al. 2022, *AJ*, 163, 174
 Banzatti, A., Meyer, M. R., Manara, C. F., et al. 2014, *ApJ*, 780, 26
 Banzatti, A., Pontoppidan, K. M., Bruderer, S., et al. 2015, *ApJL*, 798, L16
 Banzatti, A., Pontoppidan, K. M., Salyk, C., et al. 2017, *ApJ*, 834, 152
 Bast, J. E., Brown, J. M., Herczeg, G. J., et al. 2011, *A&A*, 527, A119
 Bethell, T., & Bergin, E. 2009, *Sci*, 326, 1675
 Bitner, M. A., Richter, M. J., Lacy, J. H., et al. 2008, *ApJ*, 688, 1326
 Brittain, S. D., Carr, J. S., Najita, J. R., et al. 2014, *ApJ*, 791, 136
 Canup, R. M., & Ward, W. R. 2002, *AJ*, 124, 3404
 Carr, J. S. 1989, *ApJ*, 345, 522
 Carr, J. S., & Najita, J. R. 2008, *Sci*, 319, 1504
 Carr, J. S., Tokunaga, A. T., & Najita, J. 2004, *ApJ*, 603, 213
 Ciesla, F. J., & Cuzzi, J. N. 2006, *Icar*, 181, 178
 Diaz-Rodriguez, A. K., Anglada, G., Blázquez-Calero, G., et al. 2022, *ApJ*, 930, 91
 Doppmann, G. W., Najita, J. R., Carr, J. S., et al. 2011, *ApJ*, 738, 112
 Drazkowska, J., & Alibert, Y. 2017, *A&A*, 608, A92
 Du, F., & Bergin, E. A. 2014, *ApJ*, 792, 2
 Dullemond, C. P., & Dominik, C. 2004, *A&A*, 417, 159
 Edwards, S., Fischer, W., Kwan, J., et al. 2003, *ApJL*, 599, L41
 Fang, M., Pascucci, I., Edwards, S., et al. 2018, *ApJ*, 868, 28
 Gaia Collaboration, Brown, A. G. A., Vallenari, A., et al. 2021, *A&A*, 649, A1
 Gaia Collaboration, Prusti, T., de Bruijne, J. H. J., et al. 2016, *A&A*, 595, A1
 Glasse, A. C., Atad-Ettdgui, E. I., & Harris, J. W. 1997, *Proc. SPIE*, 2871, 1197
 Gordon, I. E., Rothman, L. S., Hill, C., et al. 2017, *JQSRT*, 203, 3
 Gravity Collaboration, Perraut, K., Labadie, L., et al. 2021, *A&A*, 655, A73
 Grossman, L. 1972, *GeCoA*, 36, 597
 Head, J. W., & Solomon, S. C. 1981, *Sci*, 213, 62
 Houck, J. R., Roellig, T. L., van Cleve, J., et al. 2004, *ApJS*, 154, 18
 Ilee, J. D., Fairlamb, J., Oudmaijer, R. D., et al. 2014, *MNRAS*, 445, 3723
 Ilee, J. D., Forgan, D. H., Evans, M. G., et al. 2017, *MNRAS*, 472, 189
 Isella, A., Benisty, M., Teague, R., et al. 2019, *ApJL*, 879, L25
 Käufl, H.-U., Ballester, P., Biereichel, P., et al. 2004, *Proc. SPIE*, 5492, 1218
 Kamp, I., & Dullemond, C. P. 2004, *ApJ*, 615, 991
 Käufel, H. U., Kerber, F., Asmus, D., et al. 2015, *Msngr*, 159, 15
 Kausch, W., Noll, S., Smette, A., et al. 2015, *A&A*, 576, A78
 Kennedy, G. M., & Kenyon, S. J. 2008, *ApJ*, 673, 502
 Kopparapu, R. K., Ramirez, R., Kasting, J. F., et al. 2013, *ApJ*, 765, 131
 Koresko, C. D., Herbst, T. M., & Leinert, C. 1997, *ApJ*, 480, 741
 Kóspál, Á., Abraham, P., Acosta-Pulido, J. A., et al. 2012, *ApJS*, 201, 11
 Kraus, A. L., Ireland, M. J., Huber, D., et al. 2016, *AJ*, 152, 8
 Kruger, A. J., Richter, M. J., Carr, J. S., et al. 2011, *ApJ*, 729, 145
 Lacy, J. H., Richter, M. J., Greathouse, T. K., et al. 2002, *PASP*, 114, 153
 Lagage, P. O., Pel, J. W., Authier, M., et al. 2004, *Msngr*, 117, 12
 Mandell, A. M., Bast, J., van Dishoeck, E. F., et al. 2012, *ApJ*, 747, 92
 Mandell, A. M., Drake Deming, L., Blake, G. A., et al. 2011, *ApJ*, 728, 18
 Marley, M. S., Fortney, J. J., Hubickyj, O., et al. 2007, *ApJ*, 655, 541
 Meijerink, R., Pontoppidan, K. M., Blake, G. A., et al. 2009, *ApJ*, 704, 1471
 Najita, J., Carr, J. S., & Mathieu, R. D. 2003, *ApJ*, 589, 931
 Pascucci, I., Banzatti, A., Gorti, U., et al. 2020, *ApJ*, 903, 78
 Pinte, C., Price, D. J., Ménard, F., et al. 2020, *ApJL*, 890, L9
 Pontoppidan, K. M., Blake, G. A., & Smette, A. 2011, *ApJ*, 733, 84
 Pontoppidan, K. M., Meijerink, R., Dullemond, C. P., et al. 2009, *ApJ*, 704, 1482
 Pontoppidan, K. M., Salyk, C., Blake, G. A., et al. 2010, *ApJ*, 720, 887
 Prato, L., & Simon, M. 1997, *ApJ*, 474, 455
 Quillen, A. C., & Trilling, D. E. 1998, *ApJ*, 508, 707
 Regály, Z., Király, S., & Kiss, L. L. 2014, *ApJL*, 785, L31
 Salyk, C. 2020, slabspec, v1.0, Zenodo, doi:10.5281/zenodo.4037306
 Salyk, C., Blake, G. A., Boogert, A. C. A., et al. 2011, *ApJ*, 743, 112
 Salyk, C., Lacy, J. H., Richter, M. J., et al. 2015, *ApJL*, 810, L24
 Salyk, C., Lacy, J., Richter, M., et al. 2019, *ApJ*, 874, 24
 Salyk, C., Pontoppidan, K. M., Blake, G. A., et al. 2008, *ApJL*, 676, L49
 Sallum, S., Follette, K. B., Eisner, J. A., et al. 2015, *Natur*, 527, 342
 Scicluna, P., Wolf, S., Ratzka, T., et al. 2016, *MNRAS*, 458, 2476
 Smette, A., Sana, H., Noll, S., et al. 2015, *A&A*, 576, A77
 Smith, R. L., Pontoppidan, K. M., Young, E. D., Morris, M. R., & van Dishoeck, E. F. 2009, *ApJ*, 701, 163
 Stevenson, D. J., & Lunine, J. I. 1988, *Icar*, 75, 146
 Strom, S. E., Vrba, F. J., & Strom, K. M. 1976, *AJ*, 81, 314
 Sullivan, K., Prato, L., Edwards, S., et al. 2019, *ApJ*, 884, 28
 Wang, H., Mundt, R., Henning, T., et al. 2004, *ApJ*, 617, 1191
 Zhu, Z. 2015, *ApJ*, 799, 16
 Zhu, Z., Andrews, S. M., & Isella, A. 2018, *MNRAS*, 479, 1850